TECHNISCHE
UNIVERSITÄT
WIEN

DIPLOMARBEIT

Analysis of the type-I ELM duration regulation at ASDEX Upgrade

ausgeführt am
Institut für Angewandte Physik
der Technischen Universität Wien
und am
Max-Planck-Institut für Plasmaphysik

unter der Anleitung von
Univ.Prof. Mag.rer.nat. Dipl.Ing. Dr.techn. Friedrich Aumayr
Univ.Prof. Dipl.-Ing. Dr.techn. Elisabeth Wolfrum

durch
Richard Christian Bergmayr, BSc.
Matrikelnummer: 01526411, Studienkennzahl: 066 461

Wien, 21. Juli 2021

Friedrich Aumayr

Richard C. Bergmayr

Abstract

H-mode represents an operational mode of magnetically confined plasmas in a tokamak with enhanced confinement due to the edge transport barrier (ETB), a region of steep density and temperature gradients at a position inside the separatrix. At the edge of H-mode plasmas repetitive magnetohydrodynamic instabilities called edge localised modes (ELMs) occur. It has been shown that type-I ELMs, which cause large energy losses, vary with respect to their duration even within the same discharge. Therefore the following hypothesis is evaluated: During an ELM the absolute value of the radial electric field E_r collapses to values below 15 kV/m, which are typical for L-mode. As a consequence the ETB sustained by the radial electric field shear breaks down and strong filamentary transport is driven by the high pressure in the core. Only if E_r exceeds a critical value, the edge transport barrier builds up again and the strong transport stops. Assuming dominant neoclassical ion transport the radial electric field is set by the ratio of the edge ion pressure gradient and the density. Therefore the collisional electron-ion-heat-exchange q_{ei} at the separatrix sets the radial electric field indirectly through the ion temperature gradient and therefore regulates the ELM duration.

In this thesis 36 temporal intervals provided by 20 ASDEX Upgrade discharges are analysed, whereby for the majority of them highly resolved charge exchange recombination spectroscopy measurements are available. In order to compare various quantities at the pedestal top and the pedestal foot before and after both long and short type-I ELMs, an algorithm is developed combining the divertor current and the magnetic pick-up current signals to determine the ELM-onset and -ending times. This algorithm is implemented as a module in the application development system FusionFit.

No correlation between the collisional electron-ion-heat-exchange or the neoclassical prediction of the radial electric field and the ELM duration can be identified. Furthermore the ratio of the total collisional electron-ion-heat-exchange and the total ion heat flux is estimated for an exemplary discharge to be about 0.0046. This means that the total collisional electron-ion-heat-exchange can be neglected in comparison to the total ion heat flux. It is shown that only for 10 out of 20 temporal intervals with available data, during the sufficiently long ELMs the absolute value of the minimum of the radial electric field lies below the limit of 15 kV/m, which is typical for L-mode. According to these findings the hypothesis is refuted. However, for both the post-ELM minimum of the radial electric field and the post-ELM pedestal foot turbulence control parameter a relation with the ELM duration is found. Furthermore a correlation between the post-short ELM turbulence control parameter at the pedestal foot and the absolute value of the minimum of the radial electric field is identified. Therefore an interplay between the radial electric field and the edge turbulence or rather transport tends to regulate the respective ELM durations.

Kurzfassung

Die H-Mode stellt einen Zustand magnetisch eingeschlossener Fusionsplasmen in Tokamaks dar und zeichnet sich durch eine Randtransportbarriere aus. Diese entspricht einem Bereich steiler Dichte- und Temperaturgradienten an einer Position innerhalb der Separatrix. Am Rand von Plasmen in der H-Mode treten quasiperiodische magnetohydrodynamische Instabilitäten auf. Diese sogenannten ELMs führen zu Teilchen- und Energieverlusten des Plasmas, wobei die größten Verluste bei Typ-I ELMs auftreten. Die Dauer von Typ-I ELMs kann auch innerhalb derselben Plasmaentladung variieren. Dies gibt Anlass zu folgender Hypothese, welche in der vorliegenden Arbeit untersucht wird: Während eines ELMs bricht das radiale elektrische Feld E_r ein, sodass dessen Betrag weniger als 15 kV/m ausmacht. Solche Werte sind typisch für die L-Mode. Folglich bricht die Randtransportbarriere, welche von der Scherung des radialen elektrischen Feldes aufrecht gehalten wird ebenso zusammen und der hohe Druck im Plasmainneren verursacht starken nach außen gerichteten Transport. Nur wenn E_r einen Grenzwert überschreitet, kann die Randtransportbarriere wieder errichtet werden, sodass der starke Transport stoppt. Nimmt man dominanten neoklassischen Ionentransport an, so wird das radiale elektrische Feld durch das Verhältnis vom Ionendruckgradienten und der Dichte am Plasmarand bestimmt. Folglich reguliert der Elektronen-Ionen-Wärmeaustausch indirekt durch seinen Einfluss auf den Ionentemperaturgradienten das radiale elektrische Feld und damit auch die ELM-Längen.

Im Rahmen dieser Arbeiten werden 36 Zeitintervalle aus 20 verschiedenen ASDEX Upgrade Entladungen analysiert, wobei für den Großteil hochaufgelöste Ladungsaustausch-Rekombinations- Spektroskopie- Messungen vorhanden sind. Um verschiedene Plasmagrößen am Pedestalanfang und an einer Position innerhalb der Separatrix vor und nach einerseits kurzen und andererseits langen Typ-I ELMs zu vergleichen, wird ein Algorithmus entwickelt, welcher zur Bestimmung der ELM-Start- und -Endzeiten das Diverstrom- mit dem Pick-up-Spulen-Signal kombiniert. Dieser Algorithmus wird als Submodul der Analyseumgebung FusionFit implementiert.

Es werden keine Zusammenhänge zwischen dem stoßbedingten Elektronen-Ionen-Wärmefluss oder der neoklassischen Approximation vom radialen elektrischen Feld und den ELM-Längen gefunden. Außerdem wird das Verhältnis vom gesamten stoßbedingten Elektronen-Ionen-Wärmefluss und dem gesamten Ionenwärmefluss für eine Beispielentladung als 0.0046 bestimmt, was darauf hindeutet, dass der gesamte stoßbedingte Elektronen-Ionen-Wärmefluss im Vergleich zum gesamten Ionenwärmefluss vernachlässigbar ist. Ferner fällt der Betrag des Minimums des Profils des radialen elektrischen Feldes während langer ELMs nur in 10 von 20 Fällen mit entsprechender zur Verfügung stehender Datenlage auf einen Wert unterhalb von 15 kV/m. Die Hypothese wird daher widerlegt. Allerdings wird ein Zusammenhang mit den ELM-Längen und sowohl dem post-ELM Minimum des radialen elektrischen Feldes, als auch dem post-ELM Turbulen-

zenkontrollparameter α_t an einer Position innerhalb der Separatrix gefunden. Außerdem wird eine Korrelation zwischen α_t innerhalb der Separatrix bezogen auf Zeitintervalle nach kurzen ELMs und den Minima von E_r bezogen auf Zeitintervalle nach kurzen ELMs festgestellt. Folglich scheint ein Wechselspiel des radialen elektrischen Feldes und der Randturbulenzen beziehungsweise des -transports die ELM-Längen zu regulieren.

Contents

1 Introduction

1.1 Future carbon-free base load electricity

Due to global effects like population growth, improvements in the standards of living and the predominant economic system an ever-increasing amount of energy is needed. Certainly energy sources providing power in the future must not emit gases that trap heat in the atmosphere as this would enhance the greenhouse effect. Furthermore an ideal future energy source should be largely and at all times equally available. Eventually, an ideal energy source should not possess the disadvantages of fission power plants like the risk of meltdowns and the production of nuclear waste creating the successional problem of an ultimate storage. Fusion energy satisfies all of these criteria making it the ideal new source of carbon-free base load electricity producing no long-lived radioactive waste. Figure 1.1 shows the artistic illustration of a future fusion power plant as part of a sustainable energy mix.

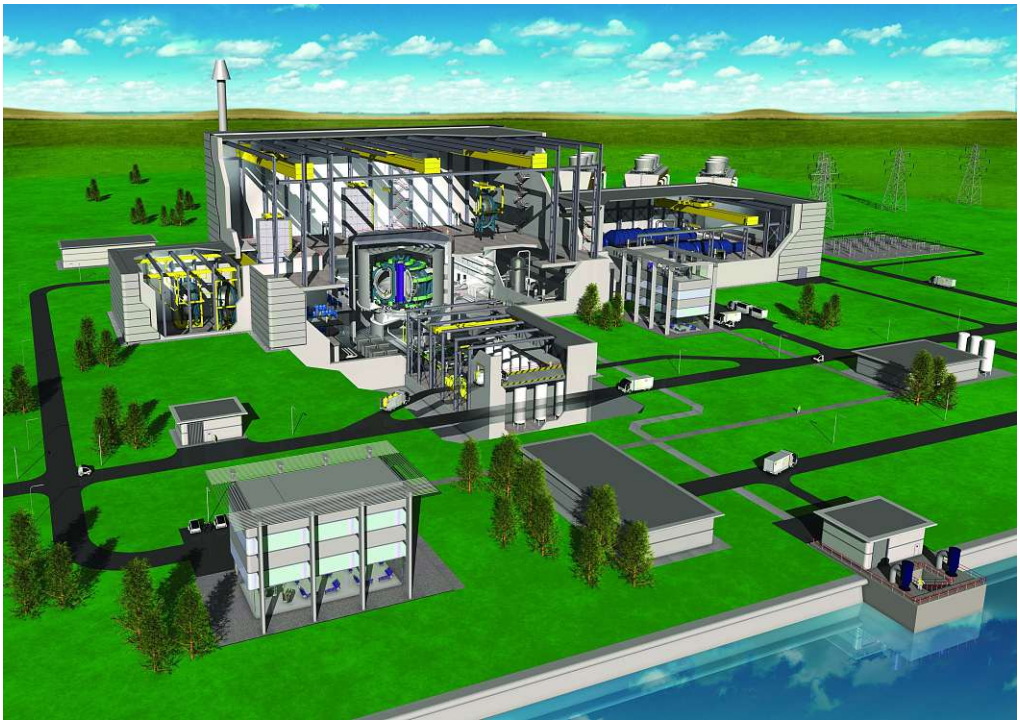

Figure 1.1: Illustration of a future fusion power plant ensuring sustainable base load electricity (taken from [1]).

Nuclear fusion is the process with which the sun delivers its energy. Controlled fusion reactions can release more than million times more energy than chemical reactions such as the burning of coal. Fusion energy is highly sustainable, as no harmful toxins like

carbon dioxide or other greenhouse gases are emitted and fusion fuels like deuterium and tritium are sufficiently available. While for instance deuterium can be distilled from all forms of water, tritium can be produced during operation using lithium. The terrestrial reserves for lithium suffice millions of years. Furthermore a fusion power plant is constructed in a way, so that a meltdown is intrinsically not possible. As reaching the necessary conditions for nuclear fusion is quite difficult, any disturbances would terminate operation. However, during operation neutrons can activate the wall material of the vessel of the fusion power plant. As the activation of the affected components is low enough for the materials to be reused or recycled within about 100 years, there is no need of an ultimate storage. Additionally there are no enriched materials in a fusion power plant that could be exploited and used as weaponry [2]. The conversion from fusion energy to electrical power is carried out conventionally using steam turbines. Even though today no fusion energy power plant is in operational state, it is expected that the first one starts operation in the 2050s [3].

1.2 Nuclear fusion

Nuclear fusion is the process of two nuclei merging to form a heavier nucleus. As the mass of the formed nucleus is less than the combined mass of the original constituents, energy is released. This process can happen, when the original nuclei get sufficiently close for the attractive strong interaction to set in. However, as shown in figure 1.2a the charged particles are repelled by the Coulomb force. Only particles possessing a sufficiently high energy can classically overcome the Coulomb barrier. The corresponding necessary magnitude of energy is about a billion degree. Due to the quantum mechanical tunnel effect the actually necessary magnitude lies in the accessible scale of about 100 million degrees [4].

Protons and neutrons, which are combined into a nucleus, hold slightly less mass than free existing ones. This difference in mass per nuclear particle corresponds to the amount of energy associated with the force holding the nucleus together. Figure 1.2b depicts the energy equivalent of the mass defect per nucleon of the elements as a function of their atomic mass. As the minimum of this curve lies around iron with mass number 56, atoms in this range are the most stable. The atoms to either side offer excess mass, which can be released in the form of energy by moving towards the minimum of the curve. While to the left hand side this happens via nuclear fusion, to the right hand side this takes place via fission, the splitting of heavy atoms to form lighter fragments [5].

As shown in 1.2b, numerous fusion reactions are possible. In the sun several processes occur as well. The most frequent form is the p-p-chain, which is depicted in 1.3a. The likelihood for a specific fusion reaction taking place is expressed as a cross section due to the necessity of an inducing collision. Figure 1.3b compares the cross sections of different fusion reactions (deuterium- deuterium, deuterium- tritium and deuterium- helium-3)

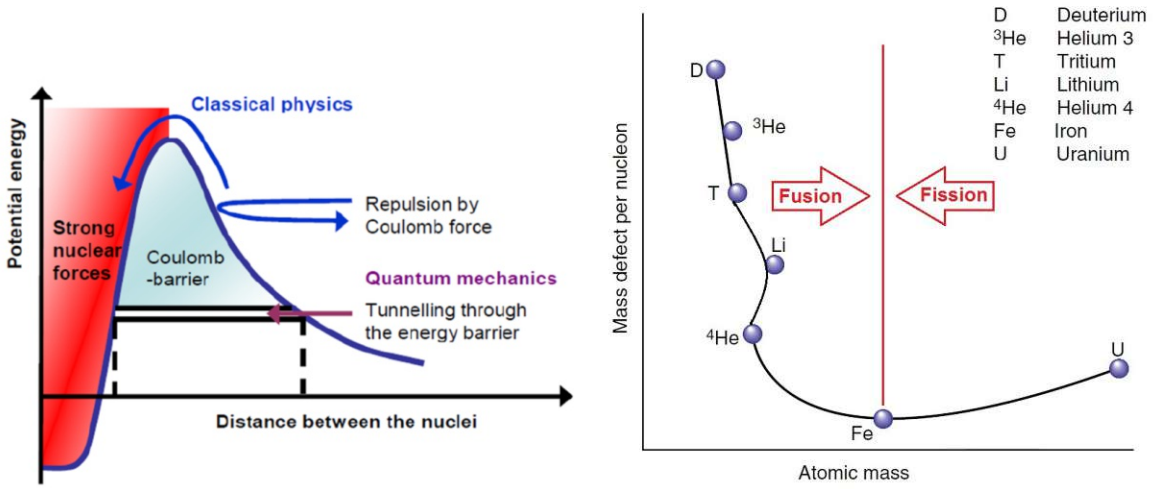

(a) (b)

Figure 1.2: Schematic illustration of the potential energy of two nuclei in dependence on their distance (taken from [6]) (a). Energy equivalent of the mass defect per nucleon of the elements in dependence on their atomic mass (adapted from [5]) (b).

for a range of energies. From an economical point of view it is favourable that the probability of fusion of deuterium and tritium is the largest at the lowest energy compared to the others. In the corresponding reaction a deuterium and a tritium fuse resulting in conventional helium, a neutron and a total energy gain of 17.6 MeV [7]:

$$ {}^{2}_{1}D \; + \; {}^{3}_{1}T \rightarrow {}^{4}_{2}He\,(3.5\;[\mathrm{MeV}]) + {}^{1}_{0}n\,(14.1\;[\mathrm{MeV}]) \tag{1} $$

Mainly due to thermal conduction and radiation the plasma loses energy. In this regard the energy confinement time τ_E is an important quantity describing the rate at which energy is lost. Nevertheless, if sufficiently numerous fusion reactions happen, a plasma doesn't expire. Therefore the Lawson criterion gives a measure of the threshold value of the product of the plasma density n, temperature T and confinement time for self-sustaining deuterium-tritium fusion reactions [5]:

$$ n\;T\;\tau_E > 3 \cdot 10^{24}\;[\mathrm{m}^{-3}\,\mathrm{eV\,s}]. \tag{2} $$

As described above, temperatures of about 100 million degrees are a necessary condition for nuclear fusion in the laboratory. At these temperatures the state of matter is plasma consisting of a gas of ions and free electrons. Different types of thermonuclear fusion concepts have been developed. In the following section it is shown, how devices of the type tokamak take advantage of the fact that plasma can be magnetically confined.

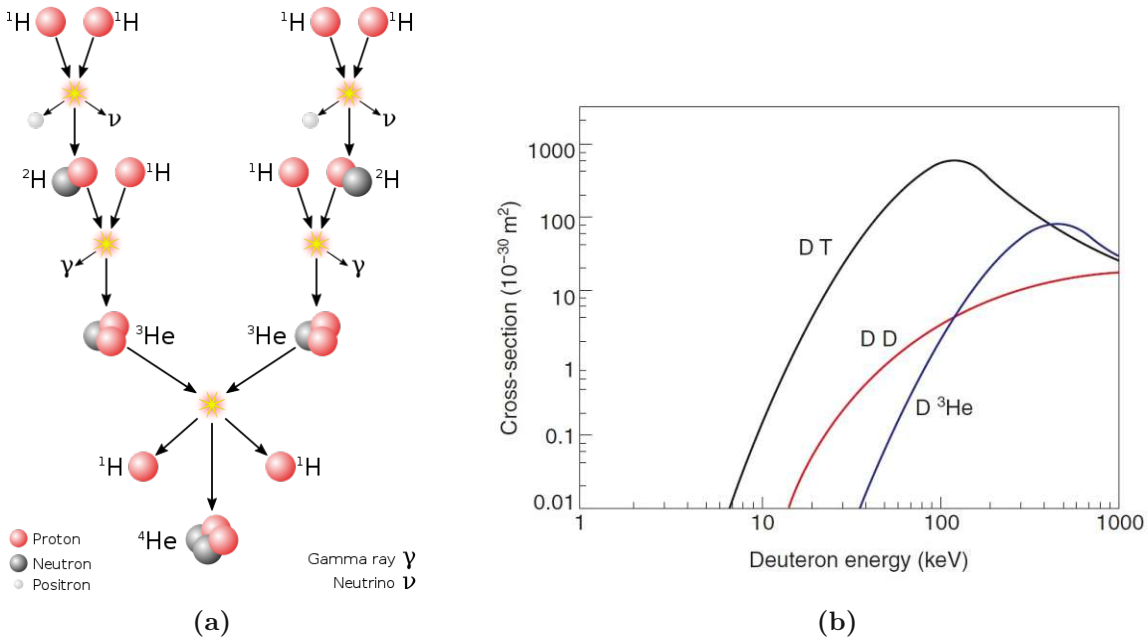

(a) (b)

Figure 1.3: Schematic illustration of the p-p-chain: all in all six ${}^1_1H$ and two ${}^2_1H$ result indirectly in two ${}^1_1H$, a ${}^4_2He$ and additional positrons, neutrinos and gamma rays (taken from [8]) (a). The cross sections of different deuterium fusion reactions for a range of energies (taken from [5]) (b).

1.3 TOKAMAK physics

The word TOKAMAK comes from a Russian acronym translating toroidal chamber with axial magnetic field [9]. Figure 1.4 schematically illustrates the composition of a tokamak and the corresponding magnetic field lines. A tokamak consists of a torus shaped vessel with coils wrapped around it, where a current is passing through. Therefore a toroidal magnetic field is induced and its strength is dependent on the radial position. As a consequence gradient $\vec{v}_{\nabla B}$ and curvature drifts $\vec{v}_{curv}$, which depend on the magnetic field $\vec{B}$ and the particle charge q, lead to a separation of charge in vertical direction:

$$\vec{v_{drift}} = \vec{v}_{\nabla B} + \vec{v}_{curv} \propto \frac{\vec{B} \times \nabla B}{qB^3}. \tag{3}$$

Hence again an electric field $\vec{E}$ builds up and so an $\mathbf{E} \times \mathbf{B}$ drift $\vec{v}_{E\times B}$ pushes the particles outwards in horizontal direction:

$$\vec{v}_{E\times B} = \frac{\vec{E} \times \vec{B}}{B^2}. \tag{4}$$

In order to avoid this troublesome motion at tokamak devices, inner poloidal field coils act as primary transformer circuit inducing a toroidal current in the plasma, which adds

a poloidal component to the magnetic field. Therefore the magnetic field is shaped helically and has spiral field lines wrapped around the torus shape. The supplementary positioning of the plasma is carried out by poloidal field coils [10].

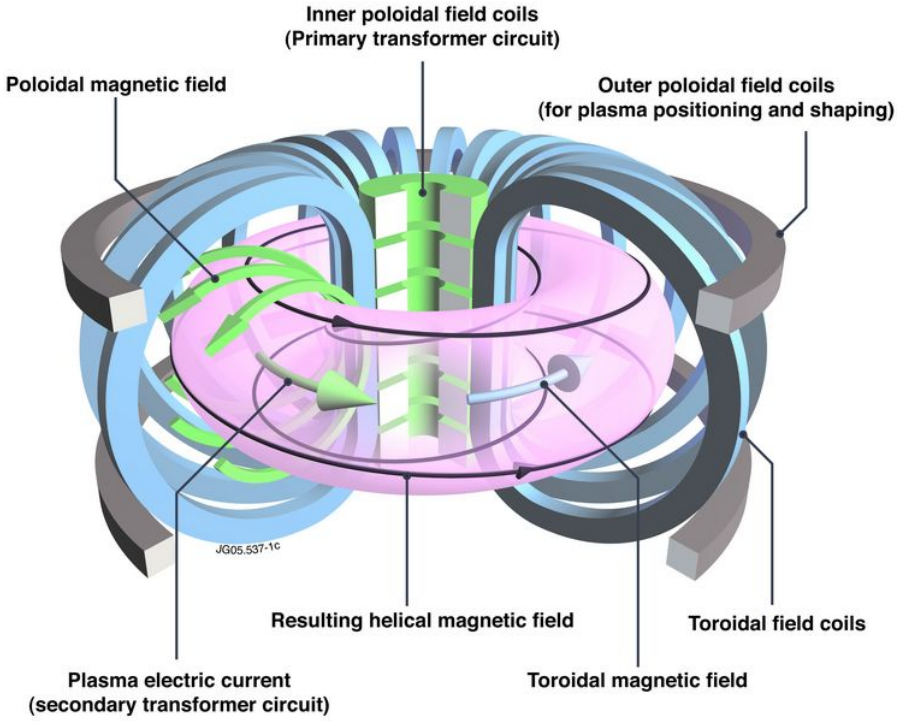

Figure 1.4: Schematic illustration of the field coils of a tokamak and the resulting magnetic field (taken from [11]).

The magnetic field lines are embedded in flux surfaces. These closed surfaces are nested within each other and the innermost is degenerated into a circle called magnetic axis. The last closed flux surface is called separatrix separating the confined region from the scrape-off layer (SOL), in which magnetic field lines intersect the wall [10]. Nowadays, most tokamaks possess a divertor as primary wall contact. The divertor is equipped with robust tiles, which can withstand the heat load of the plasma and primarily protects the main plasma from impurities sputtered from the walls of the vessel [12]. These discussed terms are illustrated in figure 1.5.

The plasmas topology can be expressed using the normalised poloidal flux labelling the magnetic flux surfaces:

$$\rho_{pol} = \sqrt{\frac{\Psi - \Psi_{axis}}{\Psi_{sep} - \Psi_{axis}}} \tag{5}$$

using the poloidal magnetic flux Ψ, the poloidal flux at the separatrix Ψ_{sep} and the poloidal flux at the magnetic axis Ψ_{axis} [13].

1.4 Plasma edge physics

In 1982 F. Wagner et al. observed a new operational regime in ASDEX divertor discharges, in which the particle and global energy confinement is significantly improved, if an input power threshold is exceeded [14]. This new operational regime was called high-confinement mode (H-mode). In contrast the operational regime below the input power threshold was named low confinement mode (L-mode). In H-mode the energy confinement time is typically enhanced by a factor of two [15] and at a position inside the separatrix very steep temperature and density gradients can be found [16]. This region is called edge transport barrier (ETB). Consequently, the ETB impedes the particle and energy flow across the plasma surface and gives rise to the improved confinement properties [17]. Figure 1.5 illustrates the comparison of the pressure profiles of the H- and L-mode against the normalised radius.

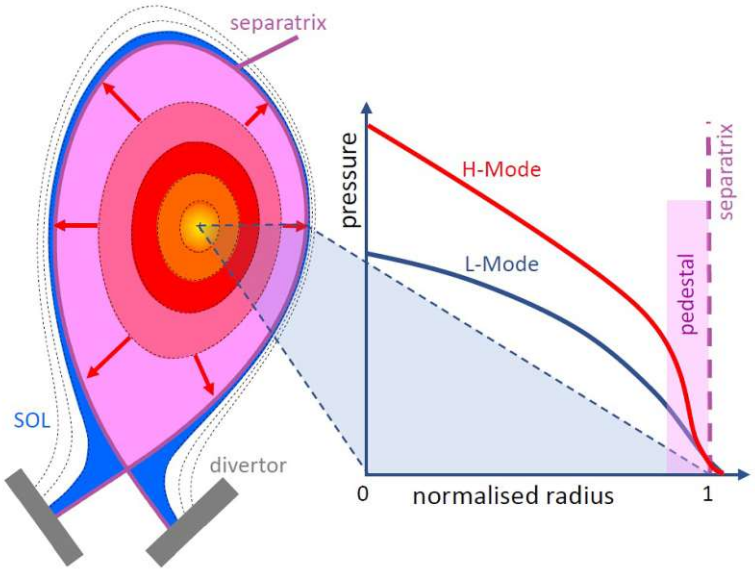

Figure 1.5: Comparison of the H- and L-mode pressure profiles against the normalised radius linked to the poloidal cross section of a divertor plasma (taken from [18]).

At the edge of H-mode plasmas edge localised modes (ELMs) occur. ELMs are repetitive magnetohydrodynamic (MHD) instabilities leading to a loss of energy and particles from the confined region on a timescale of ms [19]. The ELM-related energy losses can happen fast enough for making the peak wall energy load a major concern in large fusion devices like ITER, as it could lead to the evaporation or melting of the wall material [20].

Nevertheless, ELMs can be beneficial for H-mode operation in contemporary tokamaks as well, as they can help cleaning the accumulated impurities, which could otherwise terminate the plasma [21].

1.5 ASDEX Upgrade

In this thesis data from the tokamak ASDEX Upgrade (AUG) located at the Max Planck Institute for Plasma Physics in Garching, Germany, is analysed. ASDEX Upgrade is a medium-sized tokamak and its operation has started in 1991 following its predecessor ASDEX (Axial Symmetric Divertor EXperiment). While table 1 lists the specifications of ASDEX Upgrade, figure 1.6 shows a schematic illustration of the whole fusion device.

Recent experiments at ASDEX Upgrade aim to improve the physics base for ITER and DEMO with respect to their machine design and efficient operation preparation [22]. ITER is a fusion experiment currently in construction. DEMO is planned as first nuclear fusion power plant.

Table 1: Specifications and typical plasma parameters of ASDEX Upgrade [23].

technical data	
major plasma radius	1.65 [m]
minor plasma radius	0.5 [m]
maximum magnetic field	3.1 [T]
maximum plasma current	1.6 [MA]
pulse duration	<10 [s]
plasma heating	up to 27 [MW]
plasma parameters	
plasma volume	14 [m^3]
plasma mass	3 [mg]
plasma temperature	up to 100 million degree
plasma types	deuterium, hydrogen, helium

1.6 Objectives of this thesis

The main aim of this thesis is to investigate a hypothesis postulated by E. Wolfrum regarding the duration of type-I ELMs. For a detailed description of the mentioned terms the reader is referred to the subsequent section, which discusses them in detail. The underlying hypothesis states [24]:

- During an edge localised mode the absolute value of the radial electric field E_r collapses to typical L-mode values below 15 kV/m. Consequently, the edge transport

barrier, which is sustained by the radial electric field shear, breaks down and strong filamentary transport is driven by the high pressure in the core. If E_r exceeds a critical value, the edge transport barrier builds up again and the strong transport due to edge localised modes stops. Assuming dominant neoclassical ion transport the radial electric field is set by the ratio of the edge ion pressure gradient and the density and hence both density and ion temperature gradient act as critical parameters.

- Only at high densities at which the collisional electron-ion-heat-exchange q_{ei} suffices to affect the ion temperature in a relevant manner, the ion and electron temperature gradient are closely linked. Therefore, if at a position close to the separatrix q_{ei} is so high that the ion temperature gradient and as a consequence the radial electric field is restored quickly, edge localised modes are supposed to be short.

However, another hypothesis could be that the ion temperature at the separatrix is determined by the transport rather than by the collisional electron-ion-heat-exchange [25]. In order to consider this option as well the turbulence control parameter α_t, which describes the transition from drift wave dominated turbulence to interchange dominated turbulence, is included in the analysis.

This thesis is structured in the following way: Chapter 2 discusses the most relevant physical principles and reviews the current state of research. An overview of the utilised, advanced plasma diagnostics is given in chapter 3. The applied data analysis techniques with regard to edge localised modes are described as well. While chapter 4 presents the considered database, the methodical procedure for the evaluation of the underlying hypothesis is explained in chapter 5. The results are presented in chapter 6, their discussion and comparisons to previous findings are given in chapter 7. Chapter 8 summarises the most important aspects and gives an outlook towards further research.

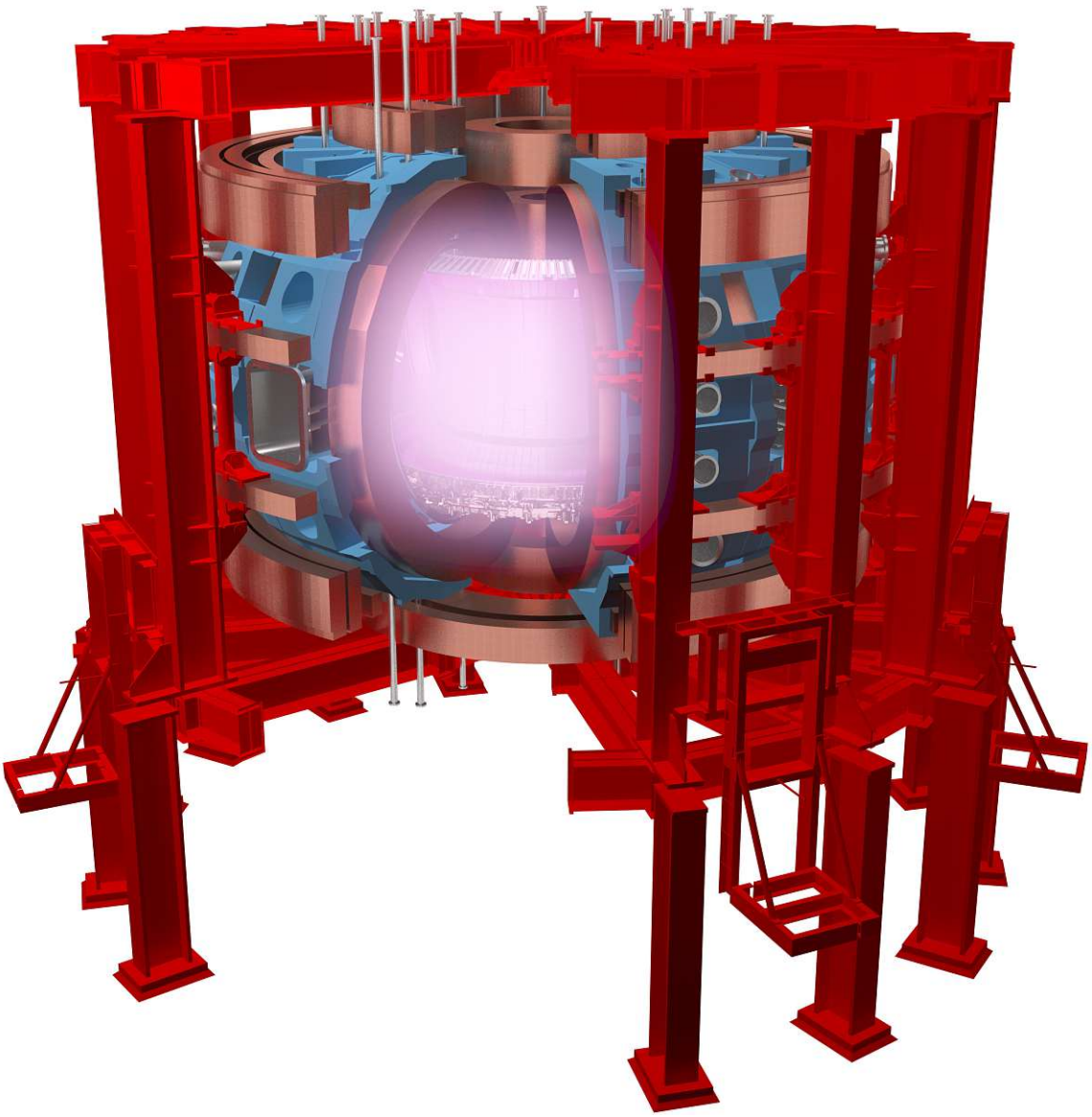

Figure 1.6: Schematic illustration of ASDEX Upgrade, a medium-sized tokamak operating since 1991. ASDEX is short for Axial Symmetric Divertor EXperiment. The actual plasma vessel (blue) is mounted on the framework (red) and the field coils are depicted in bronze. Inside the vessel the glowing plasma is shown as well (taken from [26]).

2 Theoretical background and current state of research

This chapter introduces important concepts of the theoretical background of this work and gives an overview of the current state of research. At first the formation of the ETB, which is essential for the transition to H-mode, is discussed. The enhanced confinement of H-mode usually comes at the price of the occurence of ELMs. Their characterisation, the results of previous ELM length studies and the inter-ELM recovery of the electron density, ion- and electron temperature are reviewed. As the underlying hypothesis of this thesis assumes that the collisional electron-ion-heat-exchange regulates the ELM durations, this quantity is discussed. Furthermore a parameter is introduced, which characterises the turbulence at the separatrix, since besides the hypothesis it will be considered as well, whether this is a key parameter for the regulation of ELM lengths.

2.1 Formation of the ETB

Since the publication of Biglari et al. in 1990 [27] it is believed that the formation of the ETB along with the suppression of the transport is caused by the $\mathbf{E} \times \mathbf{B}$ velocity shear, which is a consequence of the radial electric field E_r. It is widely assumed that eddies in the plasma are stretched and consequently torn apart by the shear flow. This reduces the step size of turbulent diffusion and hence the transport. Another possible mechanism for turbulence suppression is observed in fluid turbulence. In this case the flow further elongates and coils up the eddies. Therefore an energy transfer is established from the turbulence to zonal flow. Figure 2.1 compares the two possible mechanisms.

2.2 Edge localised modes

2.2.1 Characterisation

Different kinds of ELMs have been observed. Conventional classifications distinguish three types:

- **Type-I ELMs**: the repetition frequency of type-I ELMs increases with the energy flux through the separatrix ($df_{ELM}/dP_{Sep} > 0$). During the ELM there is a high level of incoherent magnetic fluctuations. The energy and particle losses of type-I ELMs are the largest [19].
- **Type-II ELMs**: necessary conditions for the appearance of these small, high-frequency ELMs are a high density and a high triangularity [21].
- **Type-III ELMs**: the repetition frequency of type-III ELMs decreases with the energy flux though the separatrix ($df_{ELM}/dP_{sep} < 0$). During the ELM there is likewise as in type-I ELMs a high level of incoherent fluctuations [19].

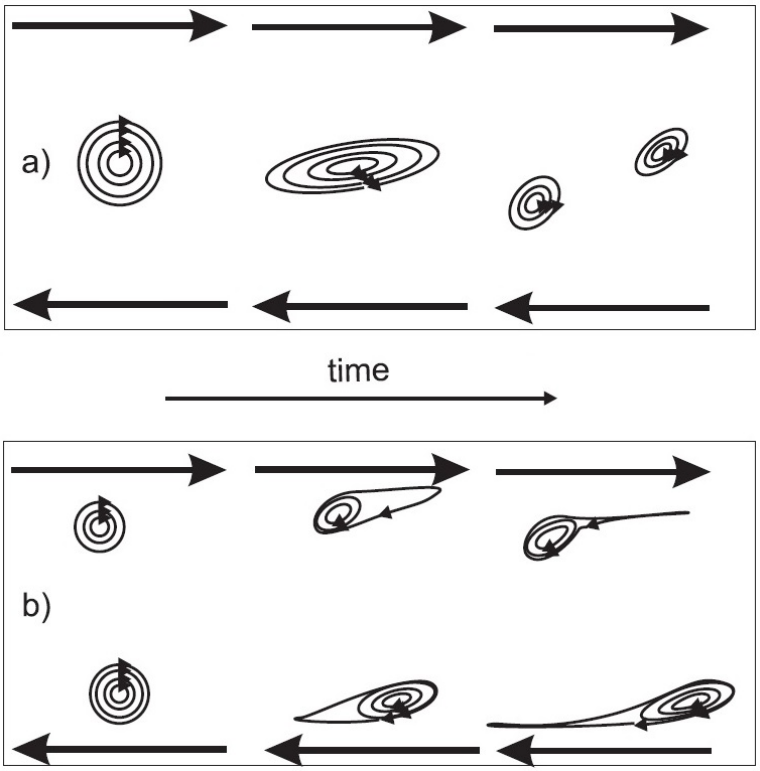

Figure 2.1: Schematic of the possible turbulence suppression mechanisms due to shear flow (adapted from [28]): Tearing apart of the eddies (a). Eddies are taken over by zonal flow (b).

At AUG the type-I ELMs show a repetition rate of typically 50 - 150 Hz and cause an energy loss of up to 10% of the total stored energy [29]. This thesis focuses on type-I ELMs. If not otherwise stated the short expression "ELM" refers to them.

An ELM is often considered as a cycle consisting of the crash itself and the recovery until the next ELM. In 2014 P. A. Schneider et al. identified three major phases [29]:

- **I**: During the ELM crash energy and particles are expelled from the plasma edge. The magnetic pick-up coils measure broad-band magnetic fluctuations from 100 to 400 kHz. In some cases a short saturation phase of varying length ($0.1 - 0.4$ ms) separates the crash phase into two distinct events (Ia) and (Ib). During the crash phase (Ib) the magnetic fluctuations stay high and the divertor current signal saturates at a high level.
- **II**: In the intermediate phase the strong magnetic perturbation of the plasma edge stops and is replaced by a quiescent phase. As the divertor plasma cools down, the thermo-currents show a decreasing signal.

- **III**: During the recovery phase the magnetic pick-up coils exhibit perturbations sized in between the ones in the first two phases. A minor temperature difference between the divertor targets causes a background signal at the divertor currents. The pedestal recovers.

In 2017 L. Frassinetti et al. showed that it is possible to observe both ELMs with phases (Ia) and (Ib) and ELMs with only phase (Ia) within the same discharge [30].

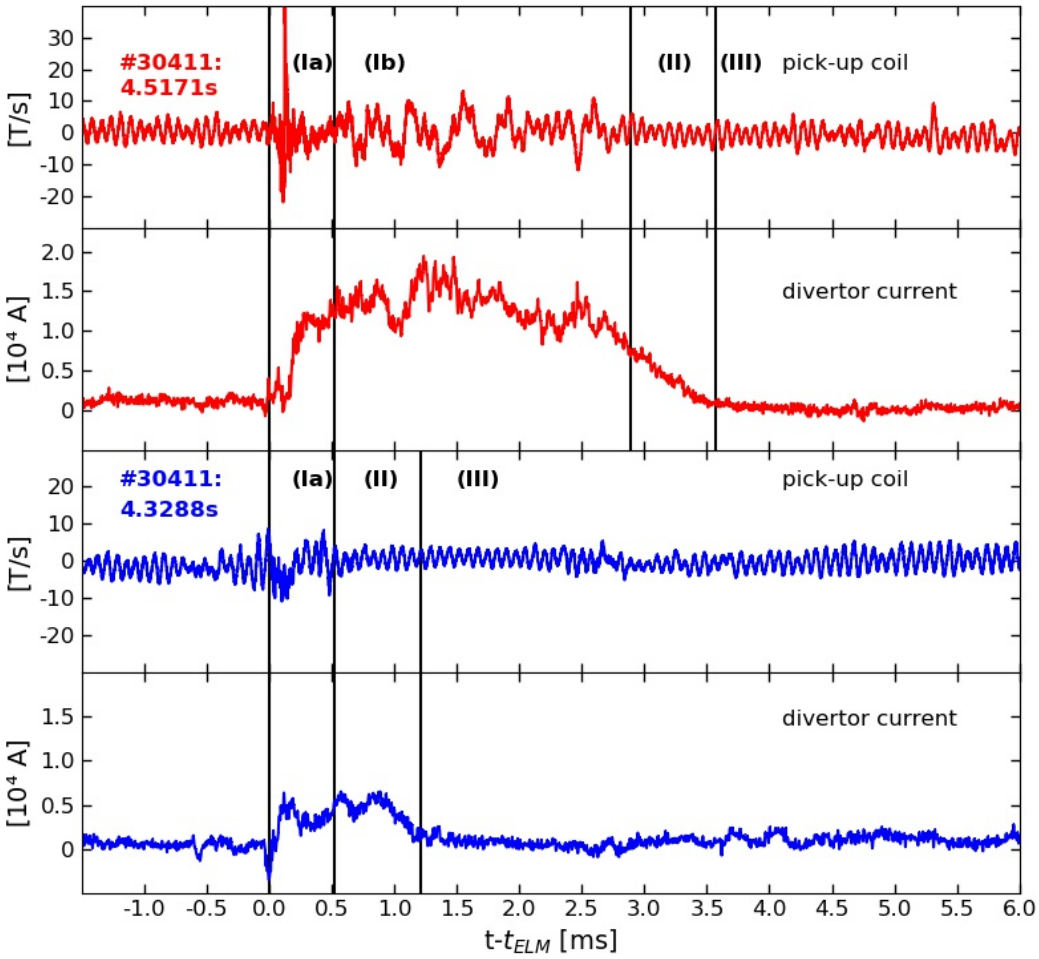

Figure 2.2: The time traces of the pick-up coil and the divertor current with regard to the respective ELM onset are shown for two ELMs of discharge #30411. The different phases of the ELMs are labelled (Ia), (Ib), (II) and (III). The upper ELM exhibits two crash phases (Ia) and (Ib), the lower ELM has only phase (Ia) (based on [29]).

Figure 2.2 compares the magnetic signature and the divertor signal of two ELMs which have happened just after each other within the same discharge (#30411). While the

upper ELM exhibits both crash phases (Ia) and (Ib), the crash phase of the lower ELM (Ia) is directly followed by the intermediate phase (II).

The second crash phase (Ib) can be reduced in size by deuterium fuelling and the increase of the separatrix density. It is possible to completely suppress phase (Ib) with the application of nitrogen seeding [31]. A nitrogen puff rate of $\Gamma = 10^{22}$ e/s acts in this regard as threshold value [30]. Thereby the first crash phase (Ia) remains mainly unchanged [29].

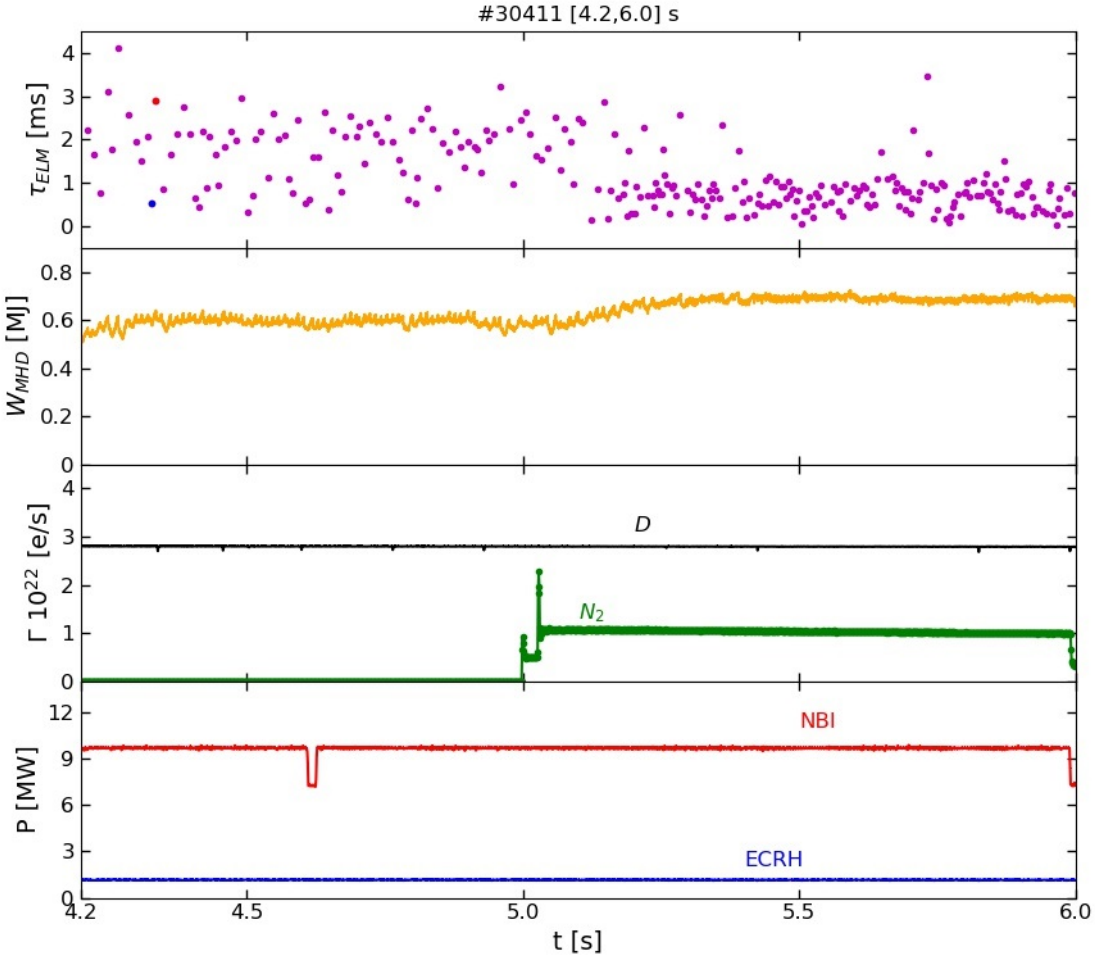

Figure 2.3: The time traces of the ELM duration, the stored energy, the deuterium (black) and nitrogen (green) flow, NBI (red) and ECRH (blue) power (based on [30]).

These findings motivate the consideration of the change in ELM length induced by nitrogen gas puffing, as shown in figure 2.3. The time traces of the ELM duration, the stored energy, the deuterium (black) and nitrogen (green) flow, neutral beam injection

(NBI, red) and electron cyclotron resonance heating (ECRH, blue) power are shown. The red and blue coloured ELM durations represent the ELMs presented in figure 2.2. For the time 4.2 - 5.0 s, when the heating power and the particle flow stay constant, the ELM lengths differ in a range of less than 1 ms up to more than 4 ms. At t = 5 s the nitrogen seeding starts and as a consequence the number of ELMs with a duration of more than 1.1 ms decreases strongly.

In accordance to [30] in the following ELMs with a duration greater than 1.1 ms will be called "long ELMs", the ones which last less than 1.1 ms "short ELMs".

2.2.2 Parameter correlations

In [30] several correlations regarding plasma parameters and the ELM lengths, which are valid for AUG, are identified: There is an inverse correlation between the fraction of the number of long ELMs over the total number of ELMs N_{long}/N_{tot} and the pedestal electron temperature $T_{e,ped}$. However, the authors highlight that their findings don't imply that the pedestal electron temperature acts as the parameter regulating the presence of the long ELMs. Rather any parameter related to the pedestal temperature, for instance the pressure, shows a similar trend. Furthermore no difference within the experimental uncertainties has been found in the pre-ELM electron temperature, electron density and ion temperature between short and long ELMs at the pedestal top.

On average the long ELMs tend to have a higher divertor temperature than the short ones before the ELM onset. While there is a positive correlation between the pre-ELM divertor temperature and the ELM energy losses for the long ELMs, no clear correlation is observed for the short ELMs. This suggests that the physics mechanism regulating the energy losses of the second crash phase is different from the mechanism regulating losses of the first crash phase [30].

2.2.3 Edge profile evolution throughout ELM cycles

In [32, 33, 34] the edge profile evolution throughout the ELM cycle of several parameters is described.

The behaviour of the ion temperature T_i at the ELM onset differs substantially from that of the electron temperature T_e. While the electron temperature close to the separatrix stays almost unperturbed, the ion temperature increases. At a position further inside towards the pedestal top region the electron and ion temperatures show a similar behaviour [32].

In 2010 A. Burckhart et al. observed a difference between the recoveries of the maximum of the gradient of pedestal parameters. The reestablishment of the maximum of

the electron density gradient ∇n_e occurs on a shorter timescale than the respective one of the electron temperature gradient ∇T_e [33].

During the ELM cycle the ion and electron temperature gradients evolve differently. While after the ELM crash the maximum ion temperature gradient ∇T_i starts immediately to reestablish, the maximum electron temperature gradient ∇T_e recovery lasts longer. Within the error bars a slight decrease of $\max(-\nabla T_i)$ is also observed before the ELM onset. Furthermore it has been found that within the uncertainties ∇T_i and ∇n_e evolve similarly after the ELM onset [32].

The temporal evolution of the edge radial electric field E_r during an ELM cycle has been studied in [34] using charge exchange recombination spectroscopy (CXRS) diagnostics with a time resolution of 2.2 ms. At the ELM crash a collapse of the edge E_r has been observed. Subsequently, the E_r recovers within 2 ms after the crash. These findings have been deepened in [32] using edge CXRS diagnostics with an unprecedented time resolution of 65 μs for the analysis of the evolution of the minimum of the measured radial electric field $\min(E_r)$ during the entire ELM cycle. The E_r shows a strong collapse at the ELM onset leading for a short time to values, which are typical for L-mode profiles. The reestablishment of the pre-ELM E_r profile is completed within 3 - 4 ms. This measurement is compared to its neoclassical prediction ($E_{r,neo} = \frac{1}{en_i}\frac{\partial p_i}{\partial r}$, where e, p_i and n_i are the elementary charge, the main ion pressure and density and $\nabla n_e/n_e = \nabla n_i/n_i$ is assumed). Within the uncertainties the measured $\min(E_r)$ and calculated $\min(E_{r,neo})$ profiles of the examined ELM crash don't show significant deviations except between 2 and 4 ms after the ELM onset.

2.3 Collisional electron-ion-heat-exchange

In a plasma two species at different temperatures exchange heat by collisions, which consequently lower the temperature difference. This process is characterised by the heat exchange time τ_{ij} and specific for the respective species i and j [7]:

$$\frac{dT_i}{dt} = \frac{T_j - T_i}{\tau_{ij}}. \tag{6}$$

For plasmas with ion charge Z the heat exchange time with regard to ions and electrons is

$$\tau_{ie} = \frac{3m_i}{2m_e}(2\pi)^{\frac{3}{2}}\frac{\epsilon_0^2 m_e^{0.5} T_e^{\frac{3}{2}}}{n_i Z^2 e^4 \ln(\Lambda)} \tag{7}$$

using the ion mass m_i, electron mass m_e, dielectric constant ϵ_0, elementary charge e and the Coulomb Logarithm $\ln(\Lambda)$ [7]. As a consequence the ion temperature rate of change can be expressed as a function of the ion density n_i, the ion charge Z and both the ion

and electron temperature:

$$\frac{dT_i}{dt} \propto n_i Z^2 \frac{T_e - T_i}{T_e^{\frac{3}{2}}}. \tag{8}$$

Assuming only a single ion species, using the quasi neutrality of the plasma ($n_e = \sum_j n_j Z_j$, whereby $\sum_j$ represents the sum over the respective ion species) and the definition of the effective charge ($Z_{eff} = \frac{\sum_j n_j Z_j^2}{\sum_j n_j Z_j}$) one obtains $n_i Z^2 \approx n_e Z_{eff}$.
The collisional electron-ion-heat-exchange q_{ei} is proportional to the product of the electron density and the heat exchange between the ion temperature rate of change:

$$q_{ei} \propto n_e^2 Z_{eff} \frac{T_e - T_i}{T_e^{\frac{3}{2}}}. \tag{9}$$

2.4 Turbulence driven transport

2.4.1 The edge plasma operational space

Due to three-dimensional simulations of the Braginskii equations two main parameters controlling transport in the edge of tokamak plasmas are identified in [35]: the MHD ballooning parameter α_{MHD} and a diamagnetic parameter α_d. These parameters span the so-called edge plasma phase space, which is illustrated in figure 2.4. In this phase space the respective regions can be distinguished, where typical L-mode levels of transport arise (L-mode), where the transport is catastrophically large (density limit) and where the L-H- transition sets in due to the formation of the transport barrier (H-mode). For large α_{MHD} a region with ideal MHD instabilities sets in.

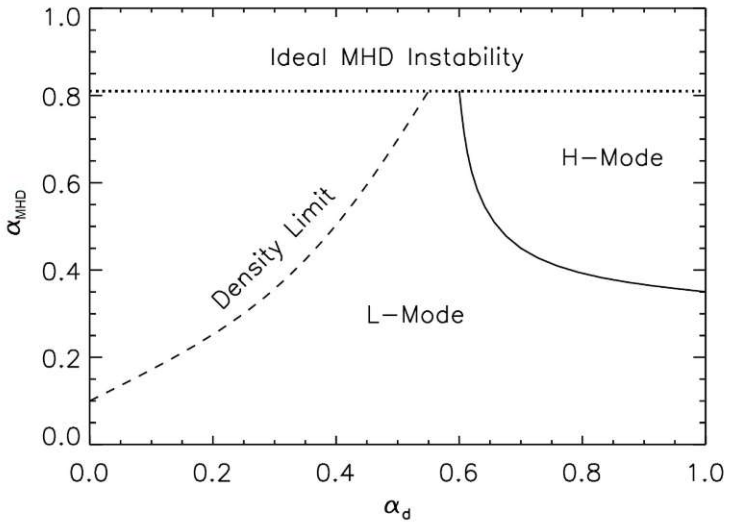

Figure 2.4: Illustration of the edge plasma phase space (adapted from [35]).

Furthermore dynamical simulations of the barrier formation process are performed in [35] confirming that the $\mathbf{E} \times \mathbf{B}$ shear effect is able to stabilise turbulence during the formation of the barrier. However, it is found that for small α_{MHD} the $\mathbf{E} \times \mathbf{B}$ shear alone does not suffice to trigger a transition due to the strong positive dependence of transport on the plasma pressure gradient.

2.4.2 Parameter description of the interchange effect on drift-wave turbulences

In [36, 37] the impact of the interchange effect on drift-wave turbulence controlled by the so-called resistive ballooning parameter $C\omega_B$ is examined. Interchange instabilities represent the magnetohydrodynamic analogue of Rayleigh-Taylor-instabilities and evolve from a deformation of the boundary between plasmas with different densities [12]. Drift waves represent a class of small amplitude, low frequency eigenmodes occurring in low beta plasmas in background magnetic fields with pressure gradients [38] and their energy source is provided by the thermal energy dissipation of the plasma as it expands across the magnetic field. Drift waves have finite wavelengths along the field lines [39].

The resistive ballooning parameter consists on the one hand of the parameter ω_B describing the strength of the interchange turbulence. On the other hand the parameter C is a measure for the normalised collisionality. While both these parameters depend on the plasma pressure gradient scale length λ_p, their product (namely the resistive ballooning parameter) does not. Hence it can be used in regression studies [40].

2.4.3 The turbulence control parameter α_t

Following the previously presented findings, in 2020 T. Eich et al. defined the turbulence control parameter $\alpha_t \equiv C\omega_B$, which describes the relative importance of the interchange effect on drift-wave turbulence and is found to be closely linked to the diamagnetic parameter α_d ($\alpha_t \propto \alpha_d^{-2}$). The turbulence control parameter α_t can be estimated within an uncertainty of less than 10 % by:

$$\alpha_t \approx 3 \cdot 10^{-18} \hat{q}_{cyl}^2 R \frac{n_e}{T_e^2} Z_{eff}. \tag{10}$$

In this expression R is the major radius, n_e is given in m^{-3}, T_e in eV and $\hat{q}_{cyl}$ can be expressed as:

$$\hat{q}_{cyl} = \frac{2\pi a^2}{\mu_0 R} \frac{B_t}{I_p} \hat{\kappa}^2 \tag{11}$$

with the minor radius a, the vacuum permeability μ_0, the toroidal magnetic field strength B_t, the plasma current I_p and

$$\hat{\kappa} = \sqrt{\frac{a + \kappa_{geo}^2 (1 + 2\delta^2 - 1.2\delta^3)}{2}} \tag{12}$$

using the elongation κ_{geo} and the triangularity δ [40].

The turbulence control parameter α_t is used in [41] to determine the separatrix density limit $n_{e,sep}^{LH} = 2.7 \cdot 10^{19}$ m^{-3} only below which it is possible that L-H- transitions can happen at AUG for the underlying plasma current and magnetic field values of $I_p = 0.83$ MA and $B_t = 2.4$ - 2.6 T.

3 Advanced utilised plasma diagnostics and data analysis

For the purpose of this thesis, namely the analysis of the pedestal and separatrix parameters before and at the end of ELMs, highly time resolved measurements of the plasma edge and the divertor have been necessary. An overview of the utilised diagnostics and their positions at a poloidal cross section of the plasma vessel are shown in figure 3.1. This chapter describes the physical principles of the respective diagnostics and the utilised data analysis methods.

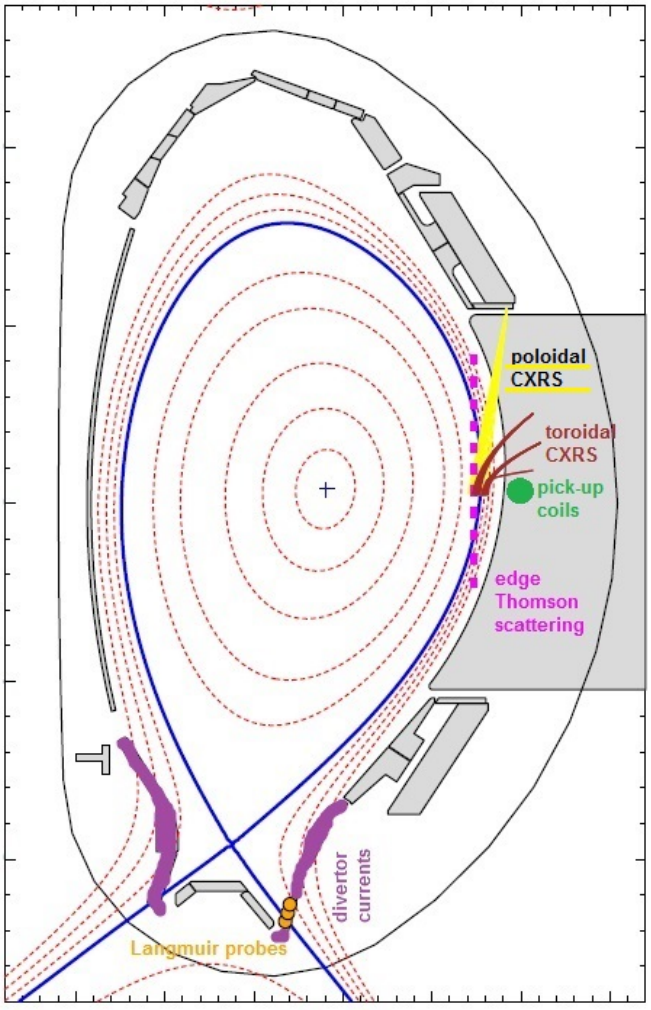

Figure 3.1: Schematic of an arbitrary plasma poloidal cross section and the utilised diagnostics: poloidal and toroidal charge exchange recombination spectroscopy, magnetic pick-up coils, edge Thomson scattering, divertor currents and Langmuir probes.

3.1 Thomson scattering

When a short laser pulse is blasted into the plasma the oscillating electric field of the electromagnetic wave causes charged particles to oscillate at the frequency of the wave. As a consequence the charge is accelerated and dipole radiation is emitted. In an electromagnetic wave field ions are only slightly perturbed due to their high mass. Therefore their contribution to the scattered power may be neglected in comparison to the contribution of the electrons. In comparison to the wavelength of the incident radiation the electrons occupy a large volume and if they are randomly spaced their individual fields add incoherently. The resulting radiated field can be considered as the product of the one of a single electron and the number of scatterers [42].

The power scattered per unit solid angle per unit frequency $d\omega$ equals

$$P = P_0 r_0^2 sin^2(\theta) n_e L S(\mathbf{k}, \omega) d\omega, \tag{13}$$

where P_0 is the total incident laser power, $r_0{=}e^2/(4\pi\epsilon_0 m_e c^2)$ is the classical electron radius in dependence on the speed of light c, θ is the angle between the incident and scattered rays, L denominates the interaction length and $S(\mathbf{k}, \omega)$ corresponds to the spectral density function. $S(\mathbf{k}, \omega)$ depends on the Fourier spectrum of the respective fluctuations causing the scattering and is a function of ω denominating the difference between the scattered and incident frequencies, the magnitude of the scattering vector k, which corresponds to the difference between the incident and scattered wave vectors and the dimensionless parameter $\alpha = \frac{1}{k\lambda_D}$ using the Debye shielding distance λ_D [7].

For the case that the Debye shielding distance is much larger than the wavelength of the laser ($\alpha \ll 1$) the Doppler shifted scattered spectrum reflects the velocity distribution of the plasma electrons. If the velocity distribution is Maxwellian, the scattered spectrum is Gaussian and its half width is proportional to $T_e^{\frac{1}{2}}$ [43].

The measurement of the absolute scattered power enables the determination of n_e, as a consequence of their direct relation [7].

At AUG the Thomson scattering diagnostics consist of a combination of a core and an edge system using Nd-YAG (neodymium-doped yttrium aluminium garnet) lasers with pulse energies below 1 J. The pulses last 10 ns and their repetition rate is 20 Hz [44].

3.2 Charge exchange recombination spectroscopy

Charge exchange recombination spectroscopy diagnostics are based on the injection of neutral beams (for instance deuterium, D) into the plasma. Hence the plasma impurity

ions A are excited by charge exchange recombination reactions. Subsequently, the excited ions decay into their initial states emitting photons $h\nu$ at the respective specific wavelengths:

$$D^0 + A^{Z+} \rightarrow D^+ + A^{(Z-1)+*} \rightarrow D^+ + A^{(Z-1)+} + h\nu. \tag{14}$$

Consequently, the ion temperature of the emitting ion species can be obtained from the Doppler width of the resulting spectra. Usually low-Z impurities are used, as they are fully stripped at tokamak electron temperatures and consequently don't radiate strongly or perturb the plasma [45].

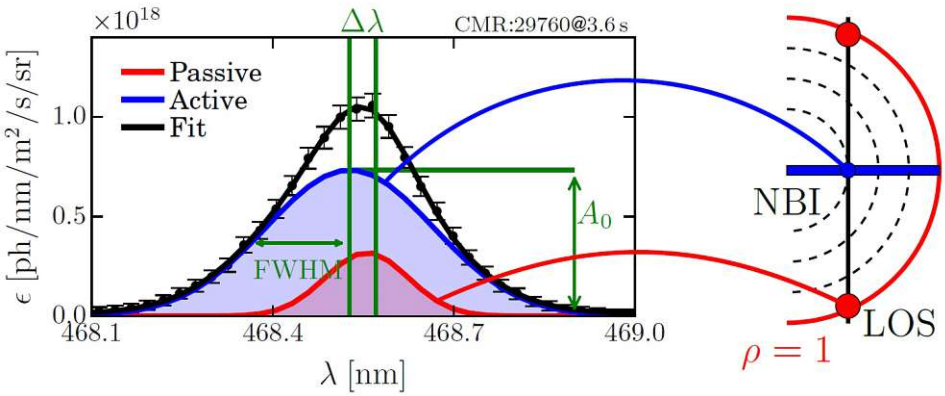

Figure 3.2: Example of a CXRS spectrum: the measured spectrum consists of an active (blue) and a passive signal (red) (taken from[13]).

Figure 3.2 shows as an example the measured spectrum of the He^{2+} $(4 \rightarrow 3)$ line emission consisting of two components. While the active signal (blue) results from charge exchange recombination with the injected neutrals in a region, where the line of sight (LOS) intersects the neutral beam, the passive signal (red) originates from neutrals in a region close to the separatrix. Assuming that the impurity ions are thermalised and consequently have a Maxwellian velocity distribution, their line emission $I_{CX}(\lambda)$ exhibit a Gaussian shape:

$$I_{CX}(\lambda) = I_0 \cdot \sqrt{\frac{m_\alpha c^2}{2\pi k_B T_\alpha \lambda_0^2}} \cdot \exp(-\frac{m_\alpha c^2}{2k_B T_\alpha} \frac{(\lambda - \lambda_0)^2}{\lambda_0^2}), \tag{15}$$

where I_0 stands for the maximum spectral radiance, m_α denominates the impurity mass, λ_0 is the unshifted wavelength and k_B the Boltzmann constant. Therefore the impurity temperature T_α can be obtained from the full width at half maximum (FWHM) of the active signal. After correction of Zeeman splitting effects, the ion temperature can be approximated by T_α [13].

The flow velocity of the impurity species projected onto the LOS can be obtained from the Doppler shift of the active signal. If the lines of sight are distributed in both the poloidal and toroidal directions, it is possible to measure both respective projections of the plasma ion flow $v_{\theta,\alpha}$ and $v_{\phi,\alpha}$. The impurity density n_α can be derived from the spectral radiance of the active charge exchange signal $I_{CX}(\lambda)$ observed by a LOS [13].

Using the radial force balance equation and the quantities obtained from measurement, it is possible to derive the radial electric field E_r, whereby ∇p_α represents the pressure gradient, Z_α the charge state, B_ϕ the poloidal component and B_θ the toroidal component of the magnetic field:

$$E_r = \frac{\nabla p_\alpha}{eZ_\alpha n_\alpha} - v_{\theta,\alpha}B_\phi + v_{\phi,\alpha}B_\theta. \tag{16}$$

At AUG several CXRS diagnostic systems are in usage. The most recent one consists of modified versions of typical Czerny-Turner spectrometers coupled with electron multiplying spectrometer charge-coupled device cameras allowing fast CXRS multiple channel measurements down to a time resolution of 10 μs at different wavelengths. Hence it is even possible to obtain profile data during short phenomena like ELMs [46].

3.3 Langmuir probes

In large tokamaks Langmuir probes are used to deduce the electron temperature and density at the plasma edge. By the application of a voltage to the electrode of the probe with respect to the vessel the resulting current is measured [7].

Figure 3.3 presents the theoretical current-voltage characteristic of a Langmuir probe. The current at the probe consists on the one hand of the ions and on the other hand of those electrons, which can reach the electrode due to their high energy, in spite of the probes repulsive potential:

$$I_{probe} = A_{probe} \cdot (-j_{i,sat} + j_{e,th} \cdot e^{\frac{e(V_{probe}-V_{plasma})}{k_B T_e}}), \tag{17}$$

where A_{probe} is the surface of the probe head, $j_{i,sat}$ the ion saturation current density, $j_{e,th}$ the thermal electron current density, e the elementary charge and k_B the Boltzmann constant [47].

The ion saturation current $I_{i,sat}$ denominates the current, at which all electrons are repelled due to a sufficiently negative potential and it is independent of the voltage. The floating potential V_f is the specific voltage at which the ion and the electron currents cancel each other [7]. If the voltage exceeds the value of the potential of the plasma V_{plasma}, successively less ions can overcome the energetic barrier and the characteristic saturates at the electron saturation current $I_{e,sat}$ [47].

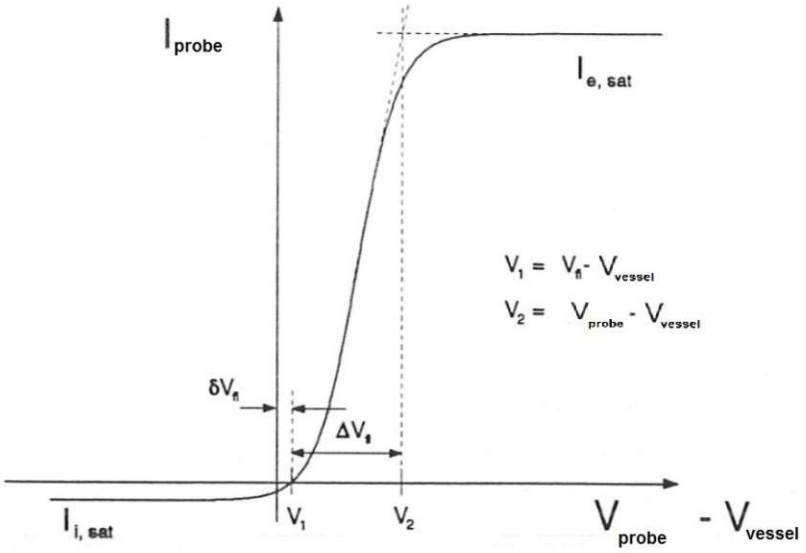

Figure 3.3: Theoretical characteristic of a Langmuir probe with all potentials denoted relative to the potential of the vessel (adapted from [47]).

The electron temperature can be derived from equation 17 and the defining condition of the floating potential ($V_f|_{I_{probe}=0}=V_{probe}$) by the elimination of the unknown quantity V_{plasma}:

$$T_e = \frac{e\,(V_{probe} - V_f)}{k_B} \cdot [\ln(1 + \frac{I_{probe}}{I_{i,sat}})]^{-1}. \tag{18}$$

The electron density can be derived from the ion saturation current using the quasi neutrality of the plasma and the acoustic velocity c_s, which again depends on the derived electron temperature [47]:

$$n_e = Z \cdot n_i = \frac{I_{i,sat}}{A_{probe}\; e\; c_s}. \tag{19}$$

At AUG numerous Langmuir probes at positions all over the plasma vessel are installed. For this work only the data of the probes placed at the divertor have been considered.

3.4 Magnetic pick-up coils

The measurement of magnetic fluctuations, for instance caused by instabilities like ELMs, can be performed using magnetic pick-up coils. According to Faraday's law of induction changes of the magnetic flux Φ_m induce a voltage signal U in the coils, which can be measured:

$$U = -\frac{d\Phi_m}{dt} = -\frac{d}{dt}\int \vec{B} \cdot d\vec{A}. \tag{20}$$

The magnetic flux is the surface integral of the normal component of the magnetic field passing through a surface A. At AUG several magnetic coils are mounted at different poloidal and toroidal positions measuring the changes of the poloidal dB_θ/dt or of the radial magnetic field dB_r/dt.

3.5 Divertor shunt currents

Due to the temperature difference between the inner and outer target plates of the divertor cassette a thermoelectric voltage is generated. This thermo-current can be indirectly measured as a voltage over a shunt [48].

At AUG the shunt currents are measured at multiple toroidal and poloidal locations and the signals are often used as ELM indicators.

3.6 ELM length analysis

A common measure for the determination of the onset of an ELM crash is the signal of the divertor currents. However, it has the disadvantage that from a physical point of view the actual crash happens slightly earlier, as the particles that are expelled from the plasma have to cover the distance between the plasma edge around the midplane and the divertor. Therefore an algorithm has been developed in the frame of this work determining the ELM crash onset and ending times combining the divertor current and the magnetic pick-up coil signals. The precise working principle of the algorithm is described hereinafter:

① Estimates of the onset and ending times of an ELM crash are determined conventionally using the rise and decay of the divertor currents signal.

② The moment 1.25 ms prior to the in ① determined onset time is calculated to account for the delay at the divertor currents. The size of the temporal value has been determined empirically and for all of the manually reviewed cases it exceeds the delay period between the magnetic pick-up coil and the divertor current signal.

③ Beginning with the in ② determined moment fast Fourier transformations of the magnetic pick-up coil data are performed using in each case a time interval of 45 μs. Successing intervals overlap by two-thirds. Collectively a period of 0.54 ms is considered in this manner. Consequently, the absolute value of the Fourier transform is calculated for each interval providing the frequency spectrum of the magnetic oscillations. Eventually, the averaged amplitude of the frequency spectrum using only the range between 100 - 200 kHz is determined together for all transformation intervals. This provides a single value as reference measure for the magnetic oscillations prior to the actual ELM onset.

④ For the entire period between the in ② determined moment and the in ① calculated ending time the respective values for the individual time intervals are determined in the same manner as in ③. However, this time the amplitude of the 100 - 200 kHz frequency spectrum is calculated and linked to its corresponding timestamp separately.

⑤ The reference amplitude value is subtracted from the actual amplitude values.

⑥ The peak value of the in ⑤ normalised amplitude signal is determined.

⑦ The ultimate change of sign of the normalised amplitude values prior to the in ⑥ determined peak value is identified. The corresponding timestamp serves as ELM crash onset time.

⑧ The timestamp of the last change of sign of the normalised amplitude values after the in ⑥ determined peak value but at the same time prior to the in ① determined estimate of the ending time is employed as actual ELM crash ending time.

⑨ The actual length of the respective ELM crash is calculated using the in ⑦ and ⑧ determined points in time.

3.7 ELM filtering

In order to consider the relevant data only with regard to the respective ELM onset or ending a basic data analysis method is applied:

- Firstly, the relevant moments with regard to the ELM cycles are determined. These are basically either the beginning or the ending of each individual ELM crash.
- Secondly, time slots with regard to the selected moments are calculated. While for the consideration of the pre-ELM crash values intervals of 3.0 ms prior up to the crash onsets are used, for the values representing the post-ELM crash values intervals from the actual ending till 3.0 ms afterwards are included.
- Eventually, the measurement data of the varying signals, for which the corresponding timestamps lie within one of the determined intervals, are used for further evaluation.

4 Database

In total 36 time intervals have been examined stemming from 20 discharges. In each of these discharges the plasma is in H-mode and type-I ELMs occur. While for most of these discharges high precision CXRS measurements are available, the discharges examined in [30], for which this is not the case, are included as well. The applied heating techniques electron cyclotron resonance heating (ECRH), ion cyclotron radio frequency heating (ICRF) and neutral beam injection (NBI) vary between the different shots. 5 discharges exhibit nitrogen (N_2) seeding and one of them additionally argon (Ar) seeding. Table 2 gives an overview of the range, the 10 - and the 90 - quantile of the plasma current I_p, the toroidal magnetic field B_t, the triangularity δ, the elongation κ_{geo} and the safety factor q_{95}.

Table 2: Range and quantile range of the plasma current, toroidal magnetic field, triangularity, elongation and safety factor in the examined discharges.

Quantity	Range	Q_{10} - Q_{90}
I_p [MW]	0.6 - 1.03	0.8 - 1.0
B_t [T]	1.9 - 2.7	2.44 - 2.62
δ	0.22 - 0.38	0.24 - 0.37
κ_{geo}	1.55 - 1.72	1.6 - 1.69
q_{95}	3.88 - 6.85	4.2 - 6.03

5 Methodical approach

This section describes the methodical procedure applied in order to obtain ELM-resolved edge profiles and consequently the ELM-resolved quantities used for the evaluation of the underlying hypothesis.

Figure 5.1 depicts the stored energy of the plasma, the plasma current, the divertor current signal, the plasma heating, the gas puff and the radial excursion of the plasma at the outer midplane of discharge #36650. The time intervals for the analysis are chosen with respect to a stable performance of these quantities. For instance for the presented discharge the selected intervals are 2.0 - 3.0 s, 4.0 - 5.0 s and 6.0 - 7.0 s. In the following procedure each time interval is examined separately.

The previously described ELM length analysis algorithm is applied combining the divertor current and the magnetic pick-up current signals providing a list of the determined ELM onset and ending times. For the next analysis steps the application development system FusionFit is used. In FusionFit it is possible to read the plasma equilibrium

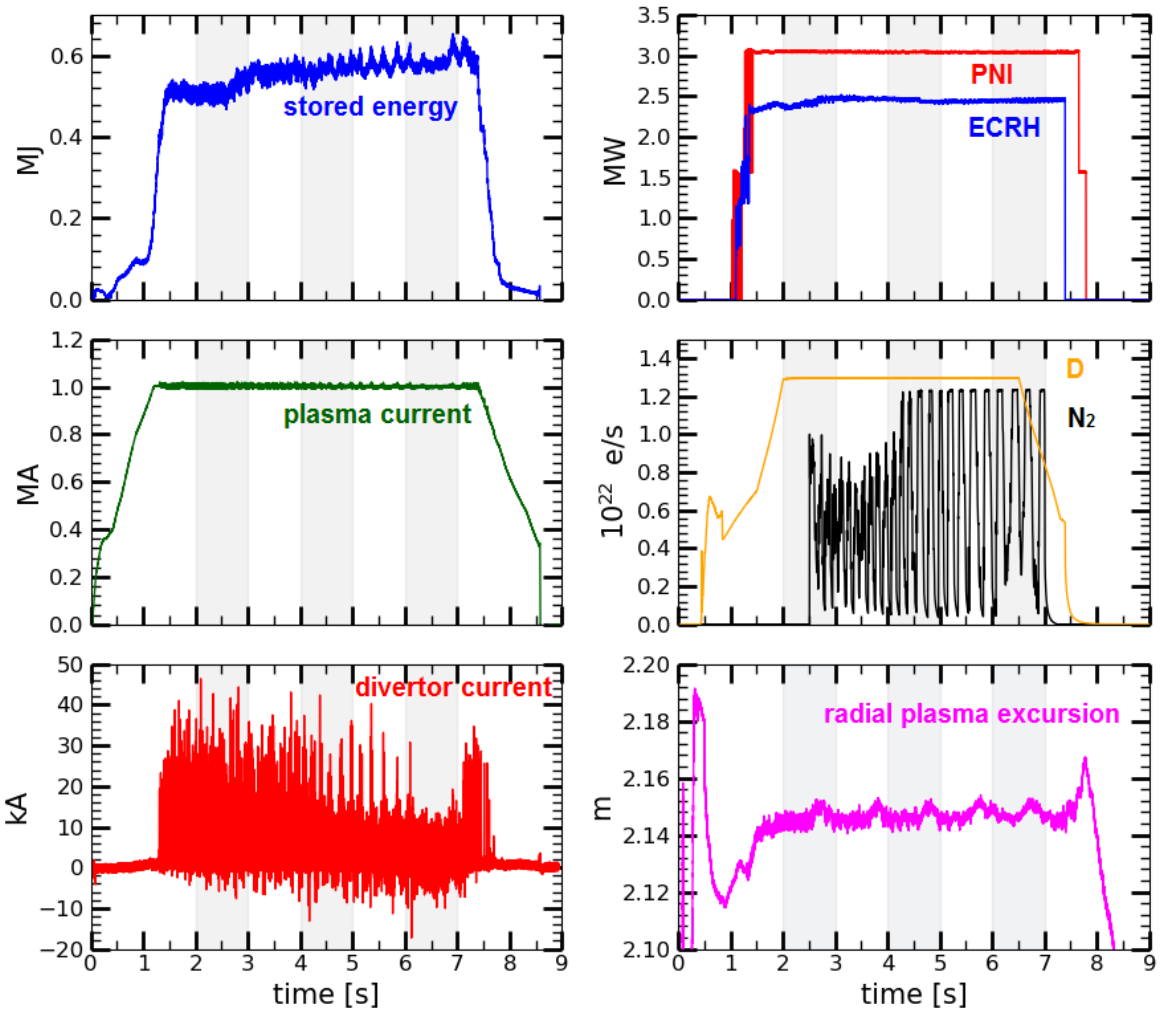

Figure 5.1: Timetraces of the stored energy of the plasma, the plasma current, the divertor current signal, the plasma heating (ECRH and PNI), the gas puff (D and N_2) and the radial excursion of the plasma at the outer midplane of discharge #36650. The time intervals used in the further evaluation have been chosen with respect to a stable performance of these quantities and are marked by shading.

and map the measured temperature and density signals to the normalised magnetic flux representation. In order to be able to select the relevant time intervals with regard to the ELM onset and ending times I developed FusionFit-modules, one that performs the ELM-time algorithm within FusionFit itself and another that can read the externally determined times. Using the onset (or ending) times the mapped profile data is filtered using only data points with a time stamp within 3 ms before (or after) the respective times. In accordance to the two-point model [12, 49] the electron temperature at AUG has a value around 100 eV at the separatrix [50]. As the separatrix values of the obtained

electron temperature profiles from the edge Thomson scattering diagnostics usually deviate from this, the signals have to be shifted. Consequently, the shifting distance is determined individually for each of the 36 investigated temporal intervals considering the pre-long ELM electron temperature profile. The respective shifting value is applied to the electron temperature profiles corresponding to time intervals after large ELMs, the electron temperature profiles corresponding to the time intervals of the short ELMs and the electron density profiles as well. Finally the obtained measurement data is fitted using a Gaussian process regression. The measured ion temperature, electron temperature and electron density profiles along with their respective fits are stored for further evaluation. Figure 5.2 exemplarily depicts the pre-ELM pedestal profiles for discharge #36650 (4.0 - 5.0 s), which are separately synchronised for long and short ELMs. The linked empty markers represent the fits and the filled markers stand for the actual measurements.

In the next step the measurement profile data is averaged in the area of $\rho_{pol} = 0.975 - 0.98$ providing a measure for pedestal top values and in the area of the pedestal foot $\rho_{pol} = 0.995 - 1.0$ for separatrix values. In figure 5.2 these intervals are highlighted in colour. Using the fit data the electron-ion-heat-exchange and the neoclassical prediction of the radial electric field are evaluated and averaged in the same areas. For the evaluation of q_{ei} Z_{eff} is an important ingredient. Because in the edge there is no reliable profile with good temporal resolution available, Z_{eff} is taken into account as value, which results from averaging over the entire pre-long ELM synchronised pedestal. Furthermore the actual E_r data provided by CXRS measurements and calculated by the radial force balance equation from the AUG database as well as the divertor electron temperature and density data is filtered with regard to the ELM onset and ending times as described in the previous section. For the resulting E_r data the minimum value of the edge profile is determined and the data points in a spatial interval of +/- 0.001 ρ_{pol} are averaged providing an estimate for the $\min(E_r)$. If the upper interval limit exceeds the separatrix coordinate, the interval of 0.998 - 1.0 is used instead. For each of the 36 temporal intervals the divertor probe with the maximal saturation current signal is determined. Consequently, its data is ELM-synchronised and averaged. Finally the turbulence control parameter is calculated using the previously determined electron temperature and density data at the pedestal top or at the pedestal foot. The remaining necessary quantities for the determination of α_t are averaged over the whole respective time interval.

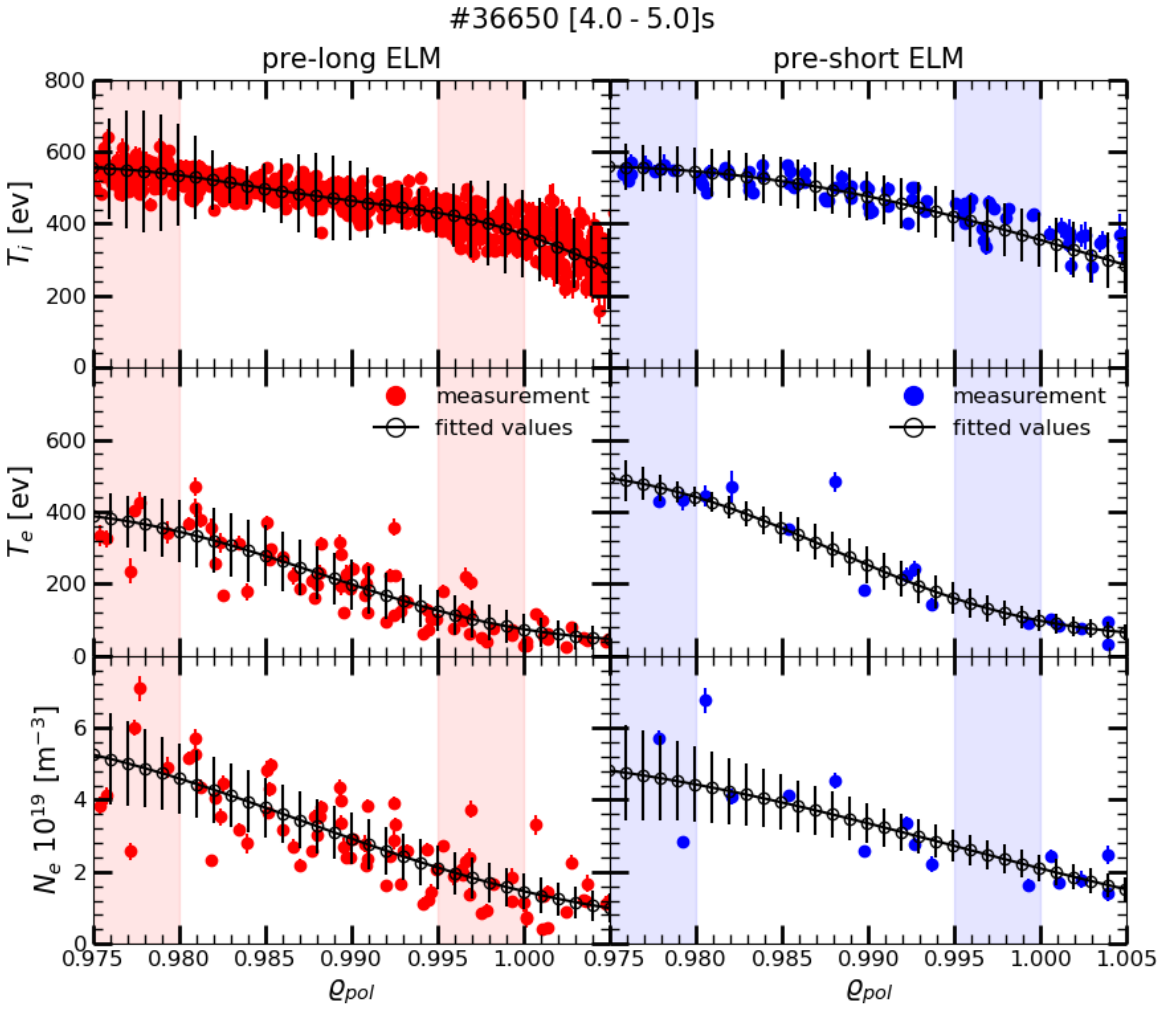

Figure 5.2: Example of ELM synchronised pedestal profiles of the ion temperature, electron temperature and electron density using pre-long (red) and pre-short ELM data (blue) for discharge #36650 (4.0 - 5.0 s), whereby the linked empty markers represent the fits. The shaded intervals are used for averaging pedestal top and pedestal foot values.

6 Correlations and Analysis

In this chapter the results of the investigation are presented. The evaluation of whether there are any trends of the ELM duration with the electron density and temperature is followed by analyses of the radial electric field and the collisional electron-ion-heat-exchange to evaluate the hypothesis underlying this work. Furthermore the turbulence control parameter is applied to investigate whether turbulence at the separatrix is crucial for the ELM duration regulation. Eventually results from Spearman's rank correlation analyses are shown.

6.1 ELM duration dependency on the electron temperature and density

This section investigates a correlation between the electron temperature or density and the average ELM duration. In order to obtain the subsequently presented data, the corresponding values of the ELM synchronised profiles have been averaged for each temporal interval as described in the previous chapter. The average ELM durations per temporal interval are evaluated separately for long and short ones. Their values are represented as colour scale. Pre-ELM data are shown as round symbols, post-ELM data as squares. Figure 6.1 compares the pre- and post-ELM electron density and temperature at the pedestal top and the respective average ELM duration. Within the available dataset no correlation can be observed between these quantities. As expected both the electron temperature and density data show slightly lower values after the ELM crashes than before them.

Figure 6.2 depicts the pre- and post-ELM electron density and temperature at the pedestal foot and the respective average ELM duration. Also in this case no difference between the values corresponding to long and to short ELMs can be detected. It can be noted, however, that for pre-ELM $T_{e,foot}$ values > 120 eV ELMs are always short. Note, that $T_{e,foot}$ is determined in the region $0.995 < \rho_{pol} < 1.0$ as described in chapter 5.

The divertor electron temperature and density data provided by the Langmuir probes and the respective average ELM duration are shown in figure 6.3. The enormous variation of the measurement data results in substantial uncertainties and as a consequence conclusions can only be drawn cautiously. Neither a difference between the long and the short ELMs, nor between the pre- and post-ELM values can be found.

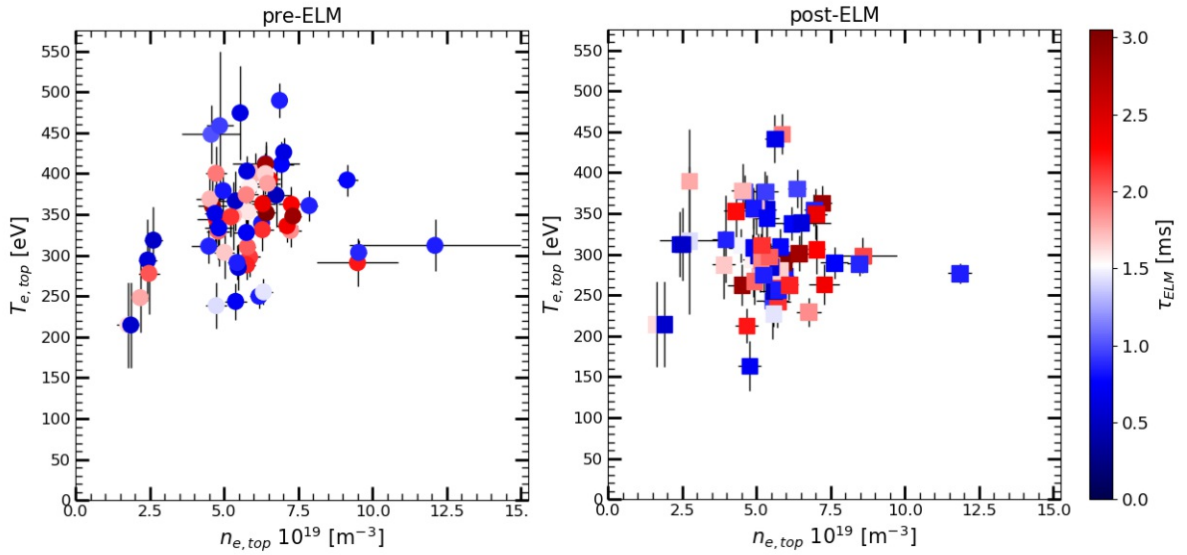

Figure 6.1: Comparison of the pre- and post-ELM electron density and temperature at the pedestal top with the colour scale representing the average ELM duration.

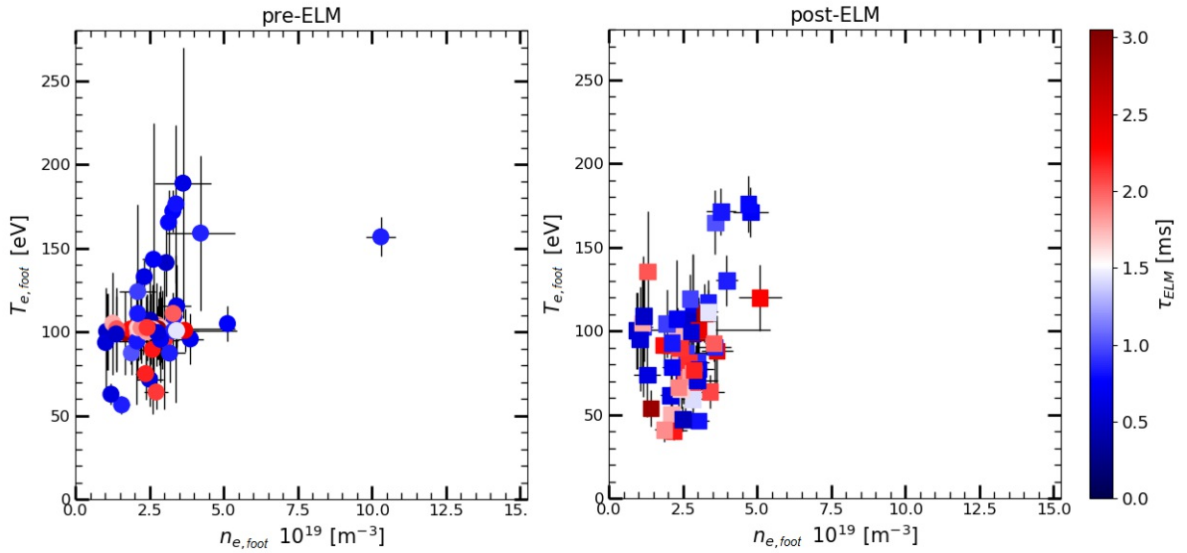

Figure 6.2: Comparison of the pre- and post-ELM electron density and temperature at the pedestal foot with the colour scale representing the average ELM duration.

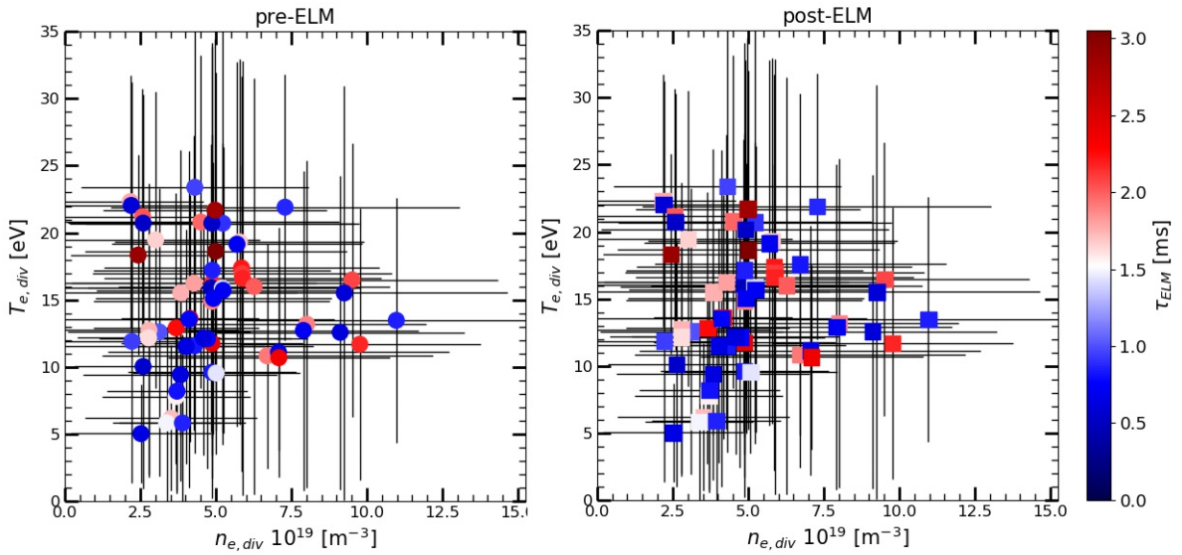

Figure 6.3: Comparison of the pre- and post-ELM divertor electron density and temperature with the colour scale representing the average ELM duration.

Furthermore it should be noted that the electron pressure has been calculated separately for long and short ELMs using the data from figures 6.1 and 6.2. For none of the evaluated cases (pre-ELM pedestal top, post-ELM pedestal top, pre-ELM pedestal foot and post-ELM pedestal foot) a difference in size between the electron pressure values calculated using data stemming from long ELMs and the values calculated with short ELM data could be found.

6.2 Radial electric field studies

This section investigates an ELM duration correlation with the radial electric field E_r and if there is evidence that the fusion plasma relapses to L-mode during the ELM crashes.

The radial electric field profile during sufficiently long ELMs is presented by means of two examples depicted in figure 6.4. For the evaluation of E_r profiles representing measurements during ELMs only data is used, which lie despite their temporal uncertainties entirely within the duration of the respective ELMs. For the considered database this is only the case for some of the long and none of the short ELMs. For 10 of the 20 available temporal intervals the radial electric field profiles during the sufficiently long ELMs show a collapse to typical L-mode profiles, in which the minimum of E_r lies above -15 kV/m. An example for this case is depicted in the cyan-coloured profile of figure 6.4. Like it is shown in the orange-coloured profile for the other 10 intervals the min(E_r) during ELMs lies well below this limit. The temporal intervals of discharge #36650 exhibit

additional N_2 gas puff and CXRS measurement data, which provide ELM-synchronised E_r profiles during long ELMs. For all of these temporal intervals the minimum of E_r lies below -15 kV/m.

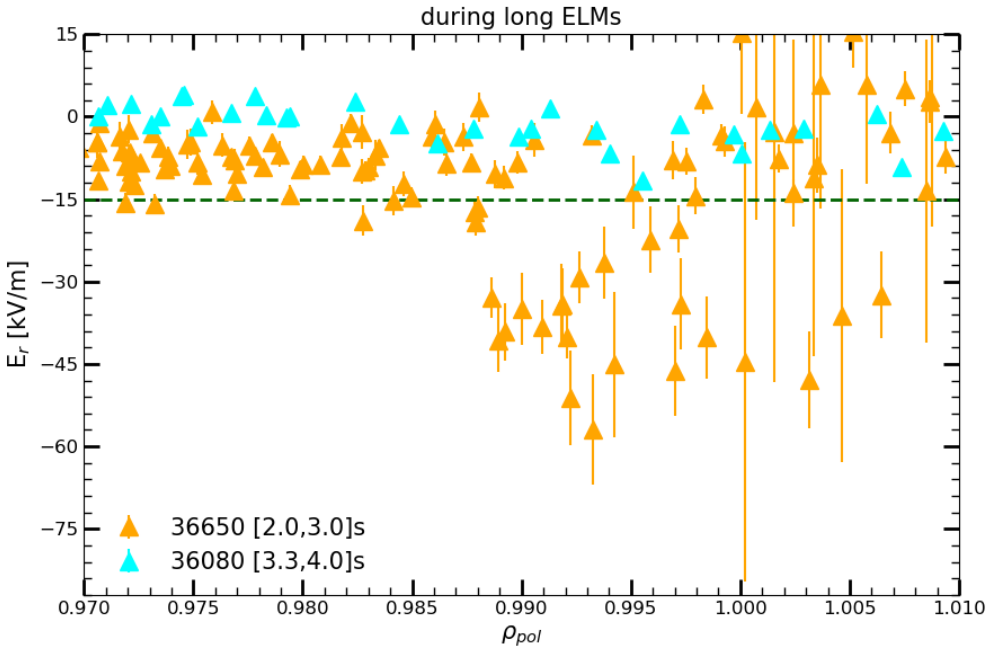

Figure 6.4: Examples of ELM synchronised radial electric field profiles of temporal intervals in which the inter-ELM min(E_r) lies above (36080 [3.3,4.0] s) and well below (36650 [2.0,3.0] s) the limit value of -15 kV/m.

In order to examine if parameters have different sizes before/after long and short ELMs, the depiction of the parameters evaluated using data synchronised before/after long ELMs versus the very same parameters evaluated using data synchronised before/after short ELMs is useful. Therefore figure 6.5 shows the pre-ELM min(-E_r) for the long ELMs versus the pre-ELM min(-E_r) for the short ELMs and the post-ELM min(-E_r) for the long ELMs versus the post-ELM min(-E_r) for the short ELMs. Pre-ELM data are shown as round symbols, post-ELM data as squares. In order to obtain the shown data points, the minimum values of the ELM synchronised radial electric field profiles have been averaged for each temporal interval as described in chapter 5. For this evaluation only temporal intervals, in which for both long and short ELMs reasonable CXRS data are available, are considered. Temporal intervals, in which additional impurities have been seeded, are colour marked in black. While it seems that the pre-ELM min(-E_r) follows no special trend with respect to the ELM duration, on average it seems that the absolute value of the minimum of the radial electric field profile tends to be bigger in size after short in comparison to after long ELMs. However, due to the uncertainties no

firm conclusion can be drawn. Moreover, the intervals with additional impurity gas puff do not stand out from the remaining intervals.

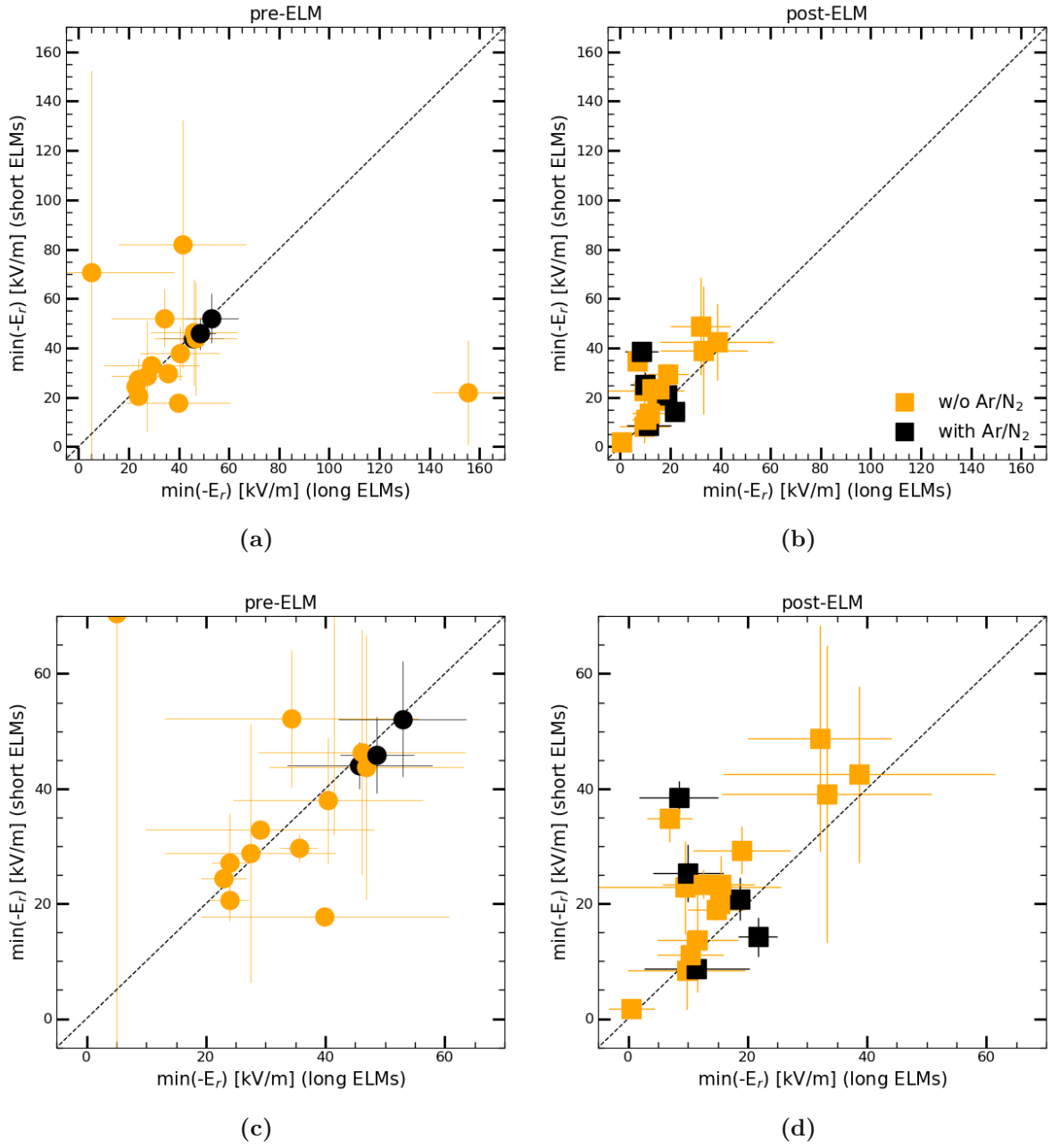

Figure 6.5: Pre-long ELM E_r versus pre-short ELM E_r (a). Post-long ELM E_r versus post-short ELM E_r (b). For clarification the lower figures depict zoomed versions of the most relevant sections of the upper ones.

Furthermore it should be noted that the method determining the min(E_r) values is for certain temporal intervals not ideally suited. As already described above the minimum value of the respective profile is determined at first and in a second step the data points are averaged in a spatial interval of +/- 0.001 ρ_{pol}. The orange data in figure 6.6 shows an E_r profile for which this procedure provides a good estimation of the minim value, as the size of the outlying data point is reduced by the data points in the neighbouring surrounding. An example of an E_r profile for which the applied method does not properly work is given by the cyan-coloured data in figure 6.6. As there are no other data points in the near surrounding of the minimum value, no averaging takes place. Therefore it is not possible to determine for sure, if the estimated min(-E_r) is an outlier or rather if it is a trustworthy data point. For example the outlier of the pre-long ELM values at the right edge of figure 6.5a is such a case. For such profiles a detailed evaluation of the proper calculation of the radial electric field profiles would be necessary. However, within the scope of this thesis such a procedure has not been possible.

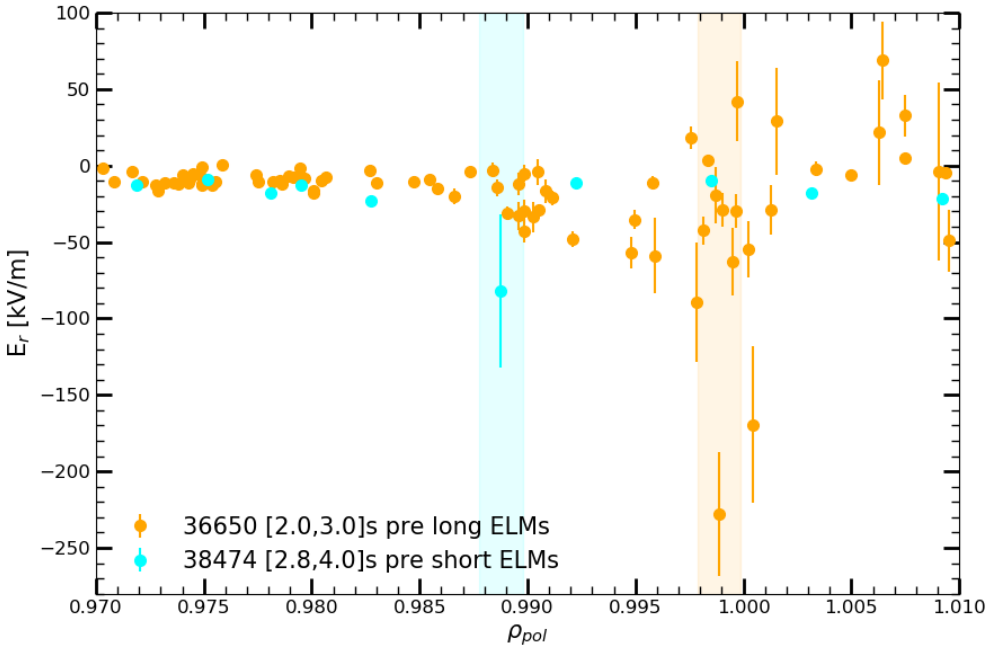

Figure 6.6: Examples of E_r profiles for which the procedure determining the previously presented min(E_r) values provides a good (orange) or rather bad (cyan) estimation. The coloured sections indicate the intervals within which the included data points are used for the corresponding averaging.

6.3 Influence of the collisional electron-ion-heat-exchange on the ELM duration

The underlying hypothesis of this thesis states that ELMs are short if the collisional electron-ion-heat-exchange q_{ei} at a position close to the separatrix suffices to restore the ion temperature gradient quickly. Therefore this section examines a possible difference of the collisional electron-ion-heat-exchange between long and short ELMs. Comparisons of q_{ei} are performed for times prior and after ELMs separately considering the pedestal top and pedestal foot data. Within the framework of this evaluation q_{ei} is only considered in each of the 36 temporal intervals, if for both long and short ELMs all of the necessary input quantities are available. Consequent error propagation can lead to large uncertainties. Data points with uncertainties much larger than their actual value are excluded from the following illustrations. Pre-ELM data are shown as round symbols, post-ELM data as squares. Temporal intervals, in which additional impurities have been seeded, are colour marked in black. Figure 6.7 compares the q_{ei} pedestal top values for long and short ELMs using pre- and post-ELM data.

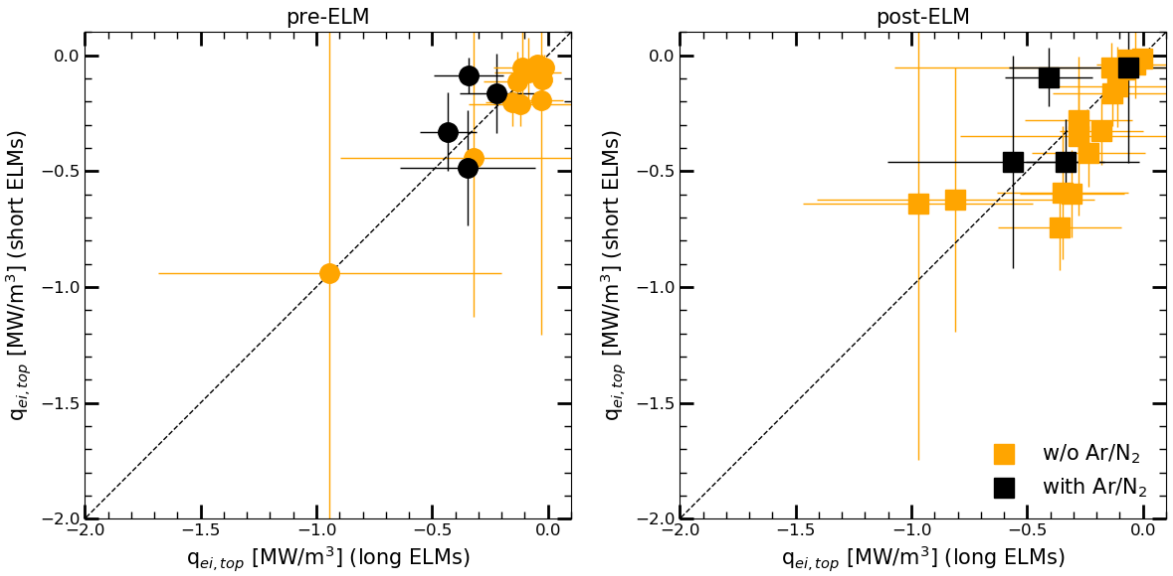

(a) **(b)**

Figure 6.7: Comparison of the long versus short ELM collisional electron-ion-heat-exchange q_{ei} for pre-ELM (a) and post-ELM (b) pedestal top values.

Figure 6.8 presents the q_{ei} pedestal foot values for long and short ELMs comparing pre- and post-ELM data. For both figures 6.7 and 6.8 no qualitative difference of the collisional electron-ion-heat-exchange between the long and short ELMs can be found.

Neither for pedestal top, nor for the pedestal foot data the intervals with additional impurity puff exhibit extraordinary behaviour.

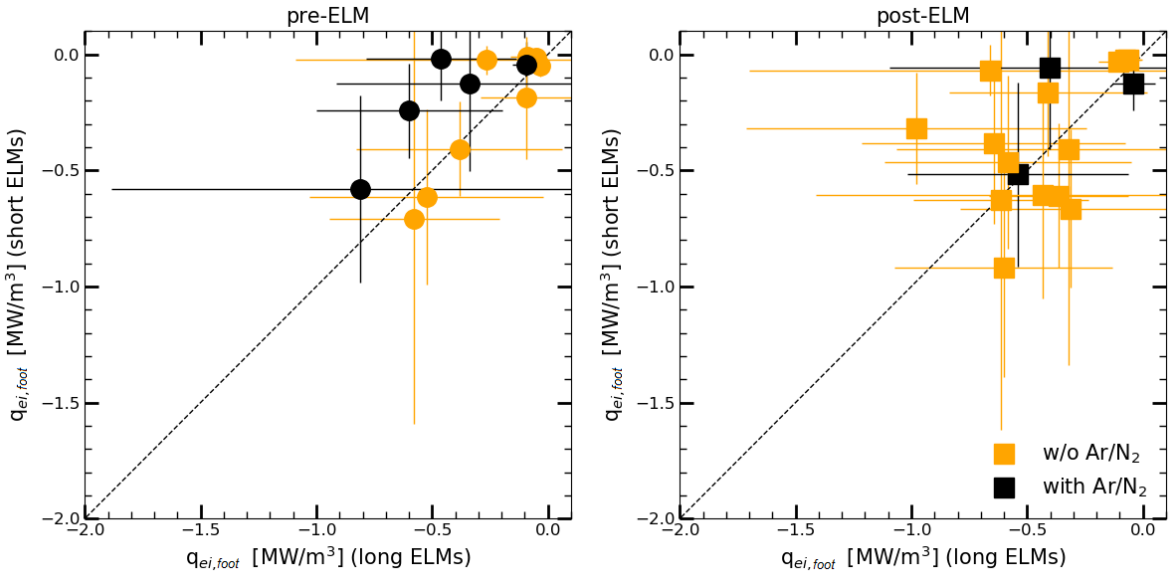

(a) **(b)**

Figure 6.8: Comparison of the long versus short ELM collisional electron-ion-heat-exchange q_{ei} for pre-ELM (a) and post-ELM (b) pedestal foot values.

This evaluation is deepened comparing the ion heat flux and the collisional electron-ion-heat-exchange. The ion heat flux q_i can be calculated using the transport coefficient χ_i [10]:

$$q_i = -n_i \chi_i \nabla T_i. \tag{21}$$

Assuming a typical transport coefficient value $\chi_i = 1.0\ \mathrm{m}^2/s$ [51] and taking for instance the pedestal foot values of discharge #36650 in the temporal interval [4.0 - 5.0]s ($n_i = 1.84 \cdot 10^{19}\ \mathrm{m}^{-3}$ and ∇T_i = -39.11 (keV)/m) this results in an estimate of the ion heat flux of 0.11 MW/m^2. The total ion heat flux Q_i can be derived from the ion heat flux by considering the plasma surface, which approximately corresponds to a cylinder barrel $A = 2a\pi R_0$ using the major and minor plasma radius of AUG

$$Q_i = q_i \cdot A = 0.58\ \mathrm{MW}. \tag{22}$$

It should be noted that for the exact determination of the total ion heat flux simulations with for instance the transport code ASTRA are necessary. The for the corresponding temporal interval estimated absolute value of the collisional electron-ion-heat-exchange at the pedestal foot is 0.05 MW/m^3. Multiplying this quantity with the volume of a

cylindrical shell with the thickness of 0.01 m using again the major and minor plasma radius of AUG one derives

$$Q_{ei} = q_{ei} \cdot dV = 0.0027 \text{ MW}. \tag{23}$$

As Q_{ei}/Q_i=0.0046, this means that the total collisional electron-ion-heat-exchange Q_{ei} is less than a two-hundredth of the total ion heat flux.

The power crossing the separatrix P_{sep} can be calculated using the total heating power P_{tot}, the time derivative of the plasma energy dW/dt and the radiated power in the main plasma $P_{rad,core}$:

$$P_{sep} = P_{tot} - \frac{dW}{dt} - P_{rad,core}. \tag{24}$$

Thereby the total heating power consists of P_{NBI}, P_{ECRH} and P_{Ohm}, the power due to NBI-, ECRH- and Ohmic heating. At the time of 4.34 s discharge #36650 exhibits the following values: $P_{NBI} = 3$ MW, $P_{ECRH} = 2.5$ MW, $P_{Ohm} = 0.85$ MW, $dW/dt = 0.85$ MW and $P_{rad,core} = 2.6$ MW. Consequently, the power crossing the separatrix is $P_{sep} = 2.9$ MW. According to the approximation of Q_i this means that about 1/5 of the power crossing the separatrix corresponds to the total ion heat flux, which empirically seems to be rather small. However, if the approximated Q_i was rather imprecise and its actual value bigger in size, this would only further reduce the ratio Q_{ei}/Q_i.

6.4 Influence of the $E_{r,neo}$ on the ELM duration

This section discusses the influence of the neoclassical prediction of the radial electric field ($E_{r,neo} = \frac{1}{en_i}\frac{\partial p_i}{\partial r}$) on the ELM duration. Following the work of M. Cavedon et al. in 2017 for the calculation it is assumed that $\nabla n_e/n_e = \nabla n_i/n_i$ [32]. The usage of the neoclassical prediction is valid due to the small contribution from the toroidal velocity at the plasma edge [52]. Only if in each of the 36 intervals for the calculation of both long and short ELM values all of the necessary input quantities are available, $E_{r,neo}$ is considered within the framework of this evaluation. Data points with uncertainties much larger than their actual value are excluded from the figures in this section. Pre-ELM data are shown as round symbols, post-ELM data as squares. Temporal intervals, in which additional impurities have been seeded, are colour marked in black.

Figure 6.9 compares the $E_{r,neo}$ pedestal top values for long and short ELMs using data prior (a) and just after (b) the respective ELMs. Due to the close alignment around the respective bisecting lines and the large uncertainties no correlation between the neoclassically predicted radial electric field and the ELM duration can be identified.

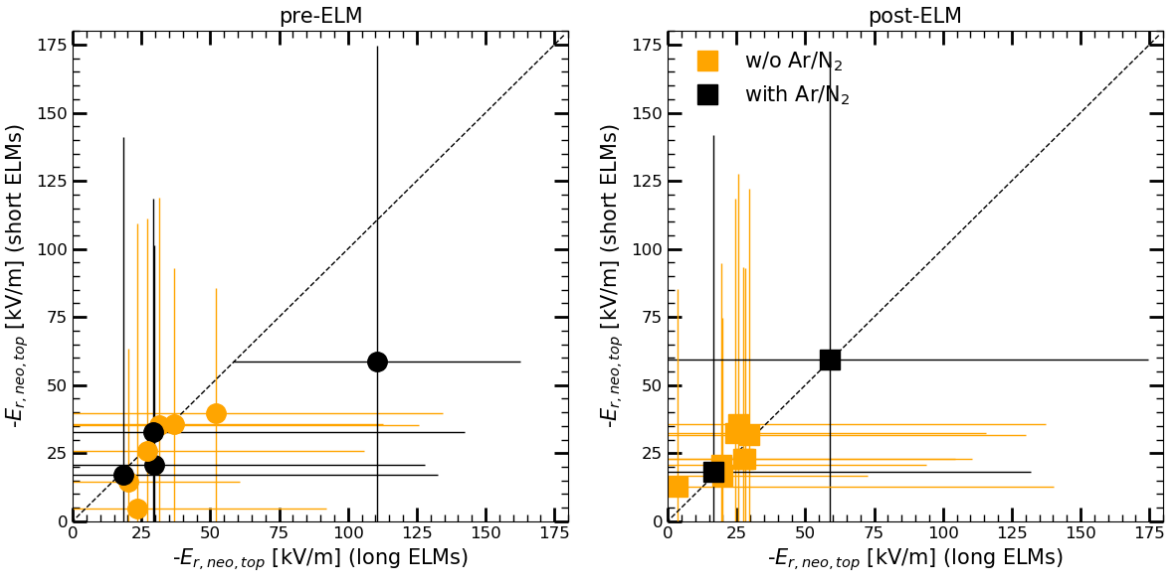

(a) (b)

Figure 6.9: Comparison of the long versus short ELM neoclassical prediction of the radial electric field $E_{r,neo}$ for pre-ELM (a) and post-ELM (b) pedestal top values.

Figure 6.10 shows the $E_{r,neo}$ pedestal foot values for long and short ELMs using data prior (a) and just after (b) the respective ELMs. Also in this comparison no correlation between the neoclassical predicted radial electric field and the ELM duration can be

identified. Neither for pedestal top, nor for the pedestal foot data the intervals with additional impurity puff exhibit extraordinary behaviour.

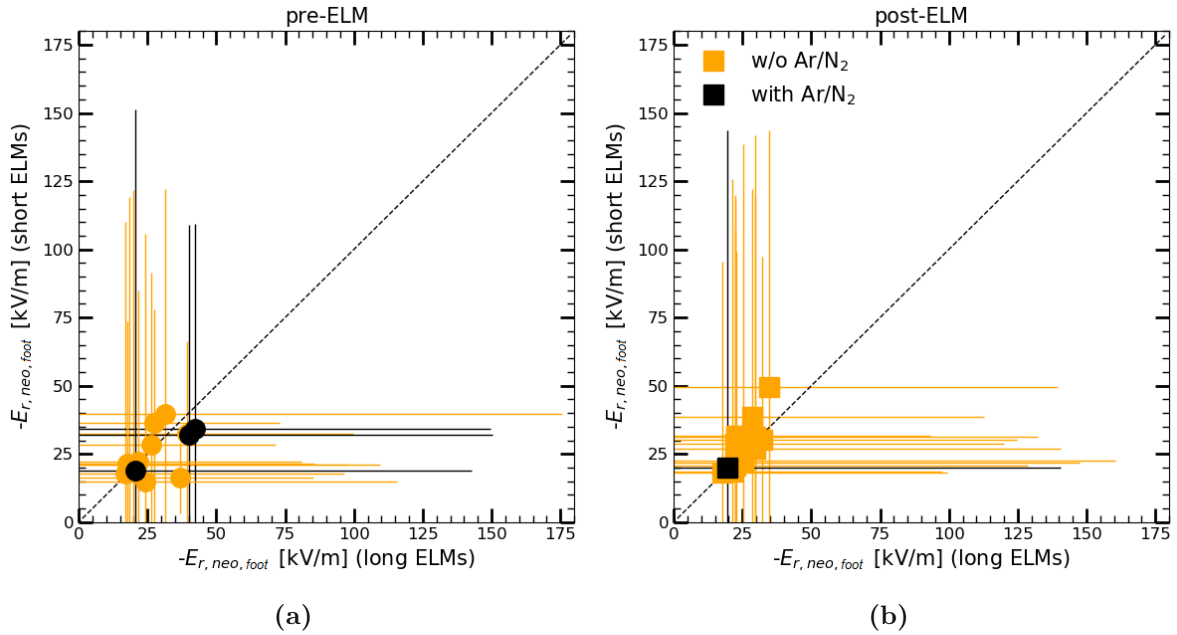

Figure 6.10: Comparison of the long versus short ELM neoclassical prediction of the radial electric field $E_{r,neo}$ for pre-ELM (a) and post-ELM (b) pedestal foot values.

As a consequence of the previously described procedure determining the neoclassical prediction of the radial electric field the evaluated uncertainties are quite large. Therefore a different methodical approach using for instance input values estimated via a maximum likelihood process would be considerable. A co-supervised Bachelor thesis following this approach is currently under progress.

6.5 Turbulence control parameter studies

This section investigates an ELM duration correlation with the turbulence control parameter α_t and its relation to the radial electric field. The temperature and density data presented in the first section of this chapter is used to evaluate α_t. As it can be observed in table 2 the minimum value of the toroidal magnetic field from the underlying database and its 10 - quantile differ strongly. Therefore the influence of the varying toroidal magnetic field on the turbulence control parameter has to be avoided. Hence the discharges with a B_t value smaller than the 10 - quantile of B_t are excluded from the analysis in this section. Pre-ELM data are shown as round symbols, post-ELM data as squares. Temporal intervals, in which additional impurities have been seeded, are colour marked in black.

Figure 6.11 shows the comparison of α_t for the long ELMs versus for the short ELMs using pre-ELM (a) and post-ELM (b) pedestal top data. Both the pre- and post-ELM values are located along the bisecting line, which means that there is no qualitative difference with regard to the ELM duration.

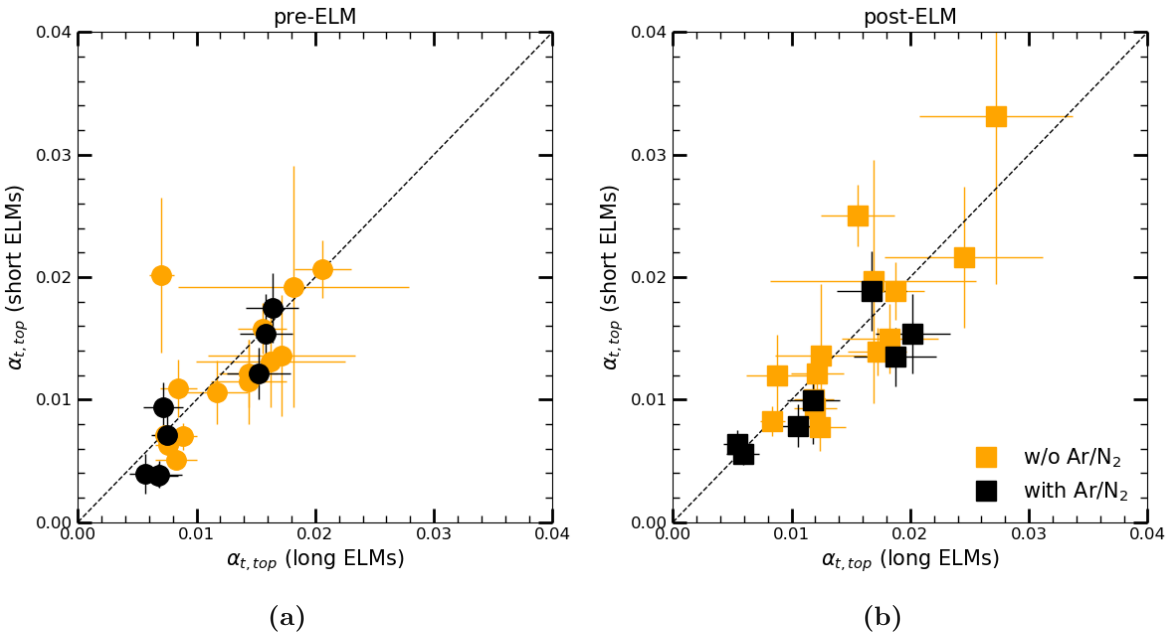

Figure 6.11: Comparison of the long versus short ELM turbulence control parameter α_t for pre- (a) and post-ELM (b) pedestal top values.

The comparisons of the pre- versus post-ELM α_t for the long ELMs versus for the short ELMs using pre-ELM and post-ELM pedestal foot data are shown in figure 6.12a and 6.12b. For better visualisation 6.12c and 6.12d depict the same relations in a smaller range. The pre-ELM values are again located around the bisecting line meaning that there is no difference between the long and short ELMs. Contrarily, the post-ELM values seem to be higher for the long ELMs in comparison to the ones corresponding to the short ELMs. This can be most clearly observed in figure 6.12d. However, neither for pedestal top, nor for the pedestal foot data the intervals with additional impurities exhibit extraordinary behaviour in comparison to the other intervals.

It is worth noting that the values presented in figure 6.11 are one order smaller in size than the values presented in figure 6.12, which accord in magnitude for instance with the data in [40]. This can be attributed to the circumstance that in figure 6.11 pedestal top data is considered. As pedestal top values surpass pedestal foot values

and as α_t is proportional to $1/T_e^2$ this leads to the different magnitudes. Furthermore it should be noted that in the database of this thesis the calculated values of $\hat{q}_{cyl}$ reach from 0.95 to 2.53, whereby the 10 - quantile is 1.48 and the 90 - quantile 1.9.

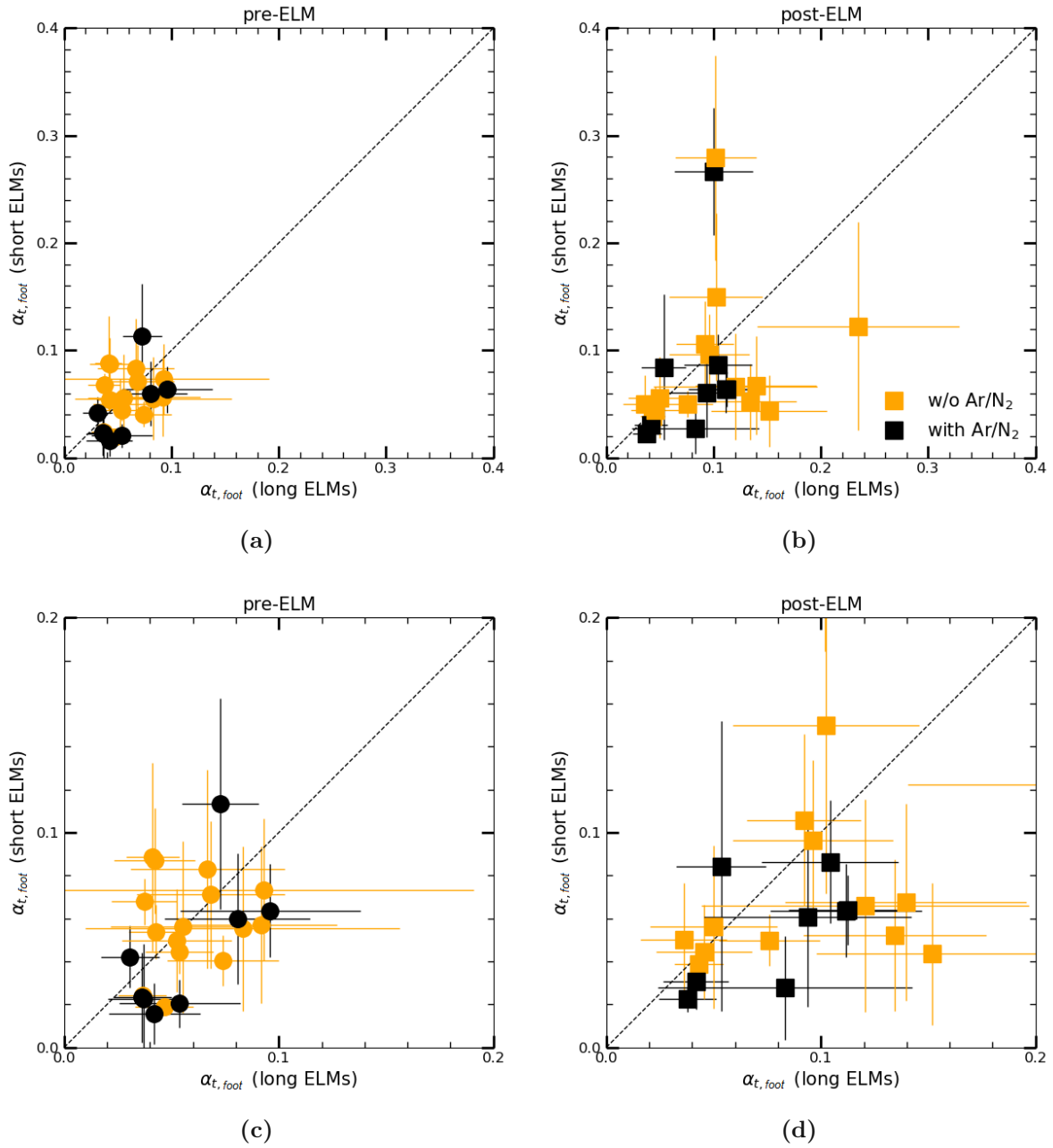

Figure 6.12: Comparison of the long versus short ELM α_t for pre- (a) and post-ELM (b) pedestal foot values. For clarification the lower figures depict zoomed versions of the most relevant sections of the upper ones.

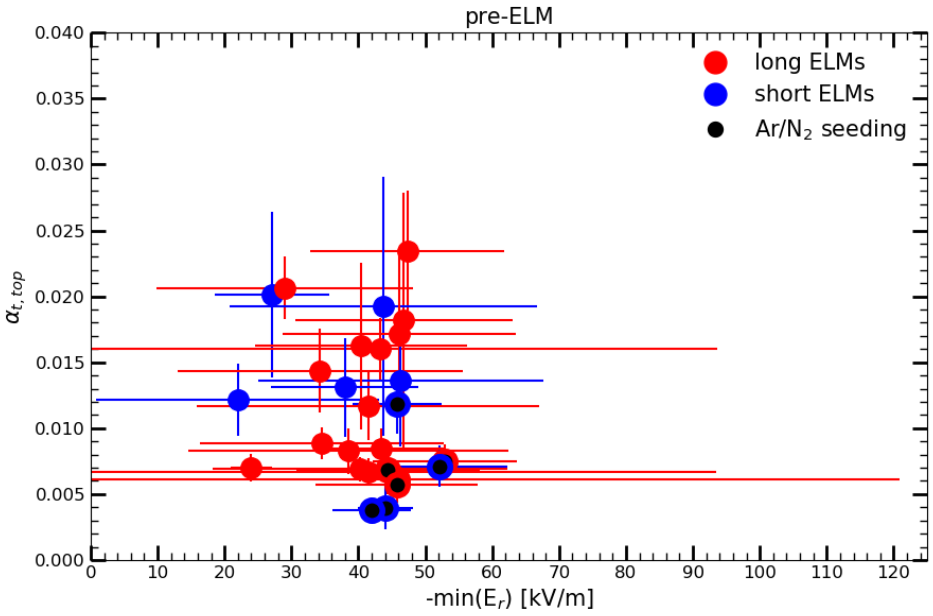

(a)

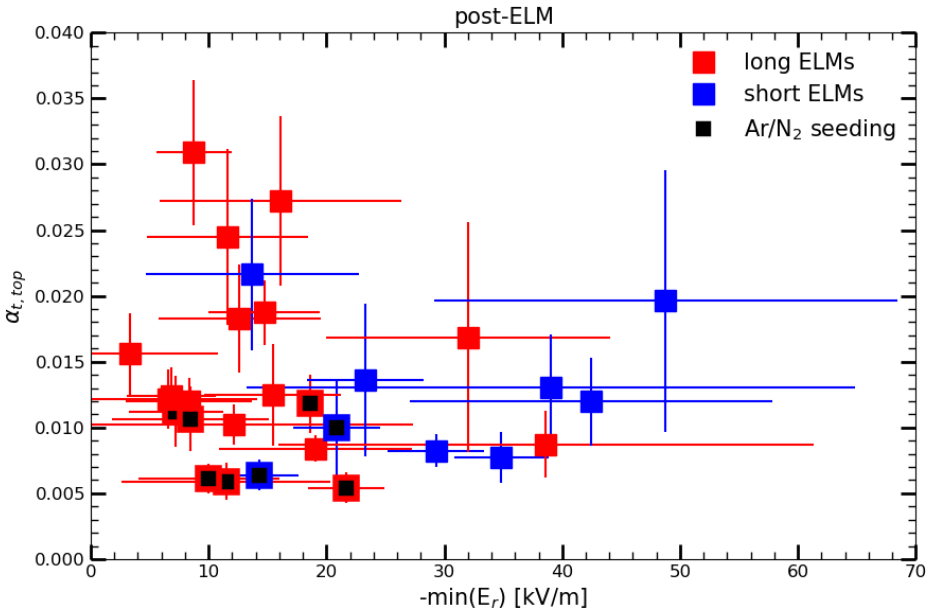

(b)

Figure 6.13: Comparison of -min(E_r) versus $\alpha_{t,}$ calculated using pre-ELM pedestal top (a) and post-ELM pedestal top (b) data.

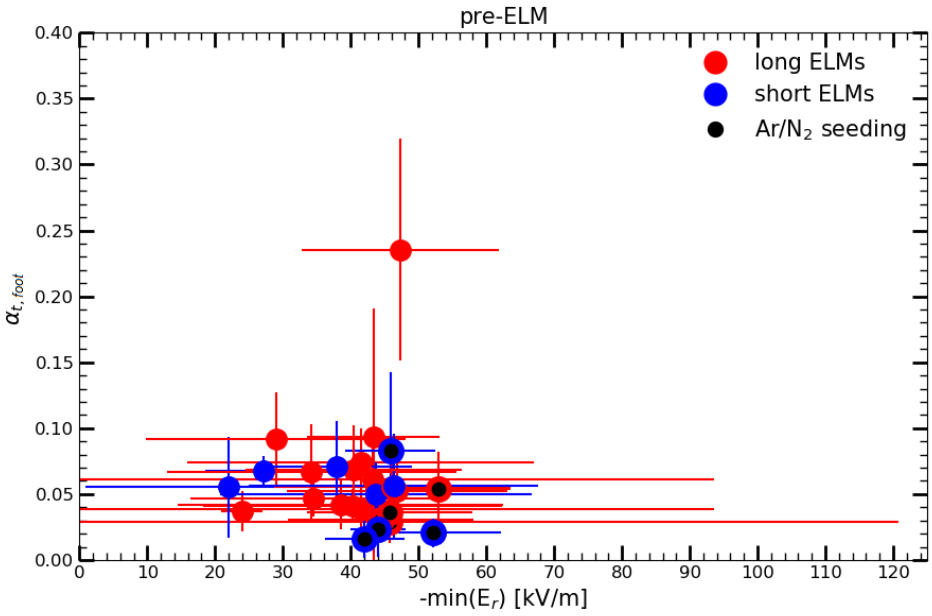

(a)

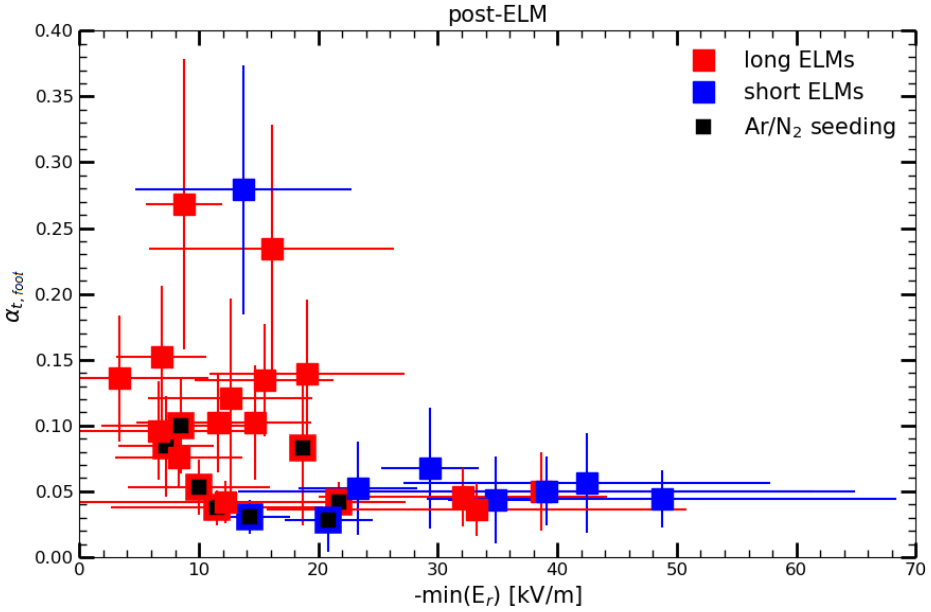

(b)

Figure 6.14: Comparison of -min(E_r) versus $\alpha_{t,}$ calculated using pre-ELM pedestal foot (a) and post-ELM pedestal foot (b) data.

Finally figures 6.13 and 6.14 compare the -min(E_r) and α_t, whereby α_t is calculated using pre-ELM and post-ELM pedestal top values and pre-ELM and post-ELM pedestal foot values separately for long and short ELMs. In order to rule out effects due to poorly available E_r profile data in the first place, min(E_r) data, for which the averaging as previously described in detail has taken place with only a single value, is excluded from the following illustrations. As the data points corresponding to the long and short ELMs mainly overlap each other, no significant correlations can be identified in the figures 6.13 and 6.14a. However, figure 6.14b seems to deepen the previously described findings: The post-ELM α_t at the pedestal foot tends to act as parameter separating the long from the short ELMs. α_t values corresponding to long ELMs occur in a range of 0.038 to 0.268. In contrast all of the α_t values corresponding to short ELMs do not exceed the limit of 0.07, with the exception of an outlier. This outlier (at α_t=0.279 and -min(E_r)=13.71 kV/m) has on the one hand a much lower electron temperature than the average post-short ELM pedestal foot electron temperature and its ELM-synchronised electron temperature pedestal profile consists only of very few measurement points. Furthermore it cannot be excluded that there is additionally a correlation with -min(E_r): Regarding short ELM values for -min(E_r) values below about 21 kV/m the corresponding α_t do not exceed a value of 0.04. Contrarily, for -min(E_r) values above 21 kV/m α_t values up to 0.067 occur. However, this consideration has to be taken cautiously due to the uncertainties. With the exception of three outliers all of the data points corresponding to long ELM values have -min(E_r) values below 22. The radial electric field profiles of the three outliers appear quite reasonable and all of them belong to the same discharge. Furthermore it is notable that all of the temporal intervals with additional impurity seeding are crowded in the lower left of the figure, namely below α_t values of 0.1 and -min(E_r) values of 22 kV/m.

6.6 Spearman correlation analysis

This section presents several Spearman correlation analyses. The analyses separately consider long, short and both long and short ELM data combined. Spearman's rank correlation coefficient is a measure of how two quantities can be linked by a monotonic function. The corresponding parameter range reaches from -1 to +1, whereby a value of +1 describes a perfect monotonic relation and a value of 0 means that there is no correlation at all. Hence Spearman's rank correlation has the advantage in comparison to Pearson correlation that not only linear, but rather any monotonic relationship can be assessed. Table 3 lists the quantities used in the correlation analyses.

Figures 6.15 - 6.20 depict the Spearman's rank correlation coefficient matrices for pre-long and -short ELM data combined (6.15), pre-long ELM data (6.16), pre-short ELM data (6.17), post-long and -short ELM data combined (6.18), post-long ELM data (6.17) and post-short ELM data (6.20). The main diagonal element values represent the cor-

relation of the respective quantity to itself and therefore naturally are +1. It can easily be seen that the correlation matrices are symmetric.

Table 3: List of quantities used in the correlation analysis along with their abbreviations. Note, that the pedestal top values are determined in the region $0.975 < \rho_{pol} < 0.98$ and the pedestal foot values in $0.995 < \rho_{pol} < 1.0$ as described in chapter 5.

Abbreviation	Quantity
τ_{ELM}	average ELM duration
B_t	toroidal magnetic field
I_p	plasma current
q_{95}	safety factor
κ_{geo}	elongation
δ	triangularity
$T_{e,top}$	pedestal top electron temperature
$T_{e,foot}$	pedestal foot electron temperature
$T_{e,div}$	divertor electron temperature
$T_{i,top}$	pedestal top ion temperature
$T_{i,foot}$	pedestal foot ion temperature
$N_{e,top}$	pedestal top electron density
$N_{e,foot}$	pedestal foot electron density
$N_{e,div}$	divertor electron density
$E_{r,neo,top}$	neoclassical prediction of the radial electric field at pedestal top
$min(E_r)$	minimum of the radial electric field profile
$E_{r,neo,foot}$	neoclassical prediction of the radial electric field at pedestal foot
$q_{ei,top}$	collisional electron-ion-heat-exchange at pedestal top
$q_{ei,foot}$	collisional electron-ion-heat-exchange at pedestal foot
$\alpha_{t,top}$	turbulence control parameter at pedestal top
$\alpha_{t,foot}$	turbulence control parameter at pedestal foot

For all of the matrices a negative correlation between the plasma current I_p and the safety factor q_{95}, as well as a positive correlation between the toroidal magnetic field B_t and the safety factor can be identified. This is trivial, since in the approximation of a linear tokamak bent from a torus to a cylinder the safety factor at the separatrix is given as $q_{95} = (2\pi a^2 B_t)/(\mu_0 R_0 I_p)$ [12].

As it can be seen in the first row of figure 6.15 the strongest (anti-)correlations with regard to the ELM duration for pre-ELM values are the $E_{r,neo,top}$ value (-0.22) and the divertor temperature $T_{e,div}$ (0.18). While the $E_{r,neo,top}$ value has an even greater anti-correlation with regard to the duration of the pre-short ELM values (-0.32), considering only the pre-long ELM values $T_{e,div}$ has a correlation coefficient of 0.3. The highest cor-

relation coefficients in dependence on the ELM duration regarding only pre-long ELM values are for the pedestal top electron density 0.37, for the divertor density 0.25, for the min(E_r) 0.21 and for the already mentioned divertor electron temperature $T_{e,div}$ 0.3. Among the highest correlation coefficients in dependence on the ELM duration regarding only pre-short ELM values are the plasma current I_p 0.48, the pedestal top ion temperature $T_{i,top}$ 0.44, the $E_{r,neo,foot}$ -0.44 and the safety factor q_{95} -0.34.

Considering figure 6.18 the strongest (anti-)correlation with regard to the ELM duration for post-ELM values is the min(E_r) value (0.52). Thereby the corresponding quantity considering only long ELMs is 0.24 in figure 6.19 and considering only short ELMs 0.52 in figure 6.20. The highest correlation coefficient with regard to the ELM duration for post-long ELM values is the pedestal top electron density $N_{e,top}$ (0.5). Among the highest correlation coefficients with regard to the ELM duration for post-short ELM values are the pedestal top ion density $T_{i,top}$ (0.55), the plasma current I_p (0.48), the $q_{ei,top}$ (-0.45) and the already mentioned min(E_r). Considering only post-short ELM quantities the correlation coefficient between the min(E_r) and the $\alpha_{t,foot}$ is -0.39.

Between the safety factor q_{95} and min(E_r), which is a negative quantity, a relatively high anticorrelation can be observed. This is true for all of the matrices.

All in all according to the Spearman rank correlation analysis a significant overall relation between the ELM duration and the collisional electron-ion-heat-exchange, the neoclassical prediction of the radial electric field or the turbulence control parameter cannot be identified.

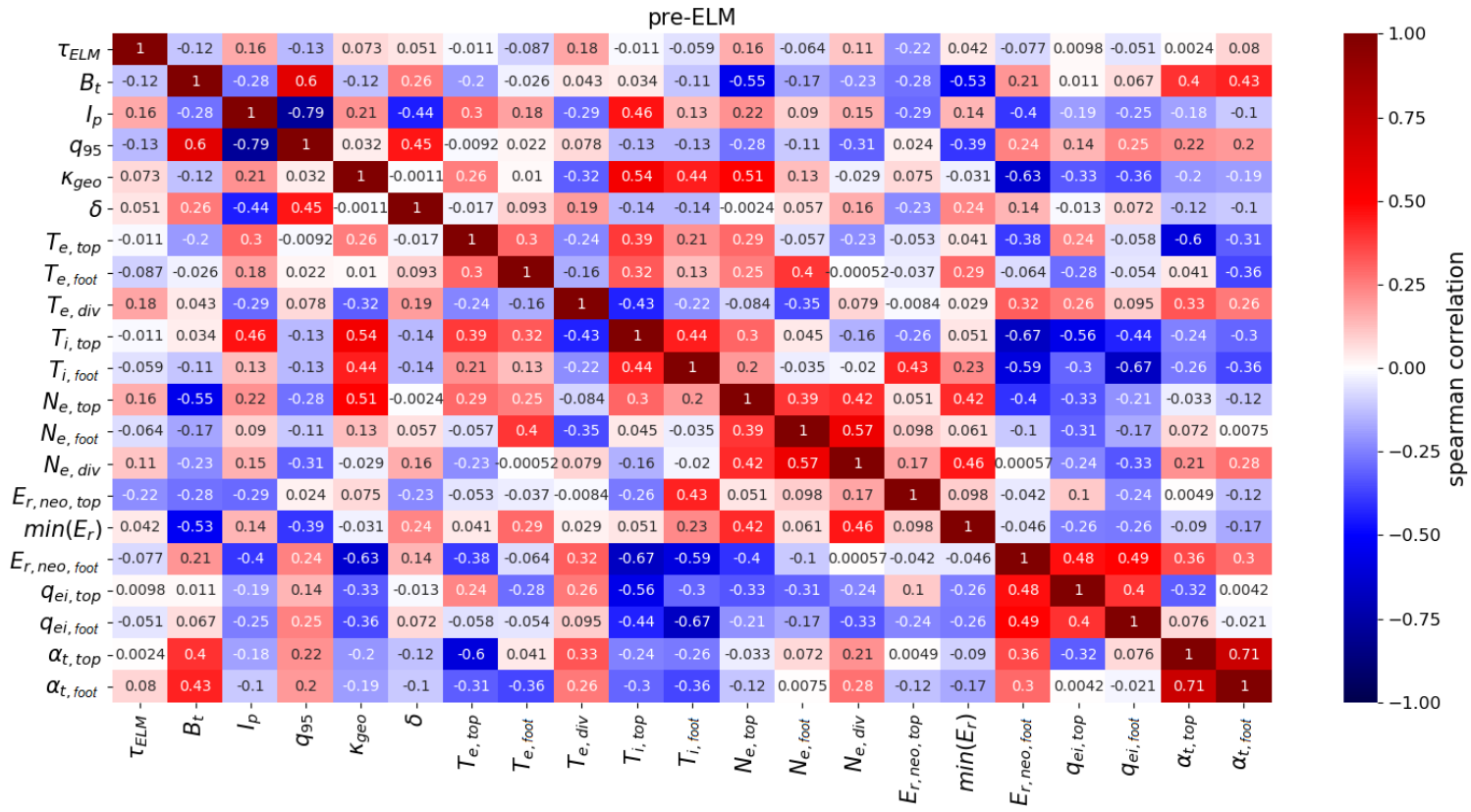

Figure 6.15: Illustration of the Spearman's rank correlation coefficient matrix for pre-ELM values measuring how two quantities can be linked by a monotonic function. The corresponding parameter range reaches from -1 to +1, whereby a value of +1 describes a perfect monotonic relation and a value of 0 means that there is no correlation at all.

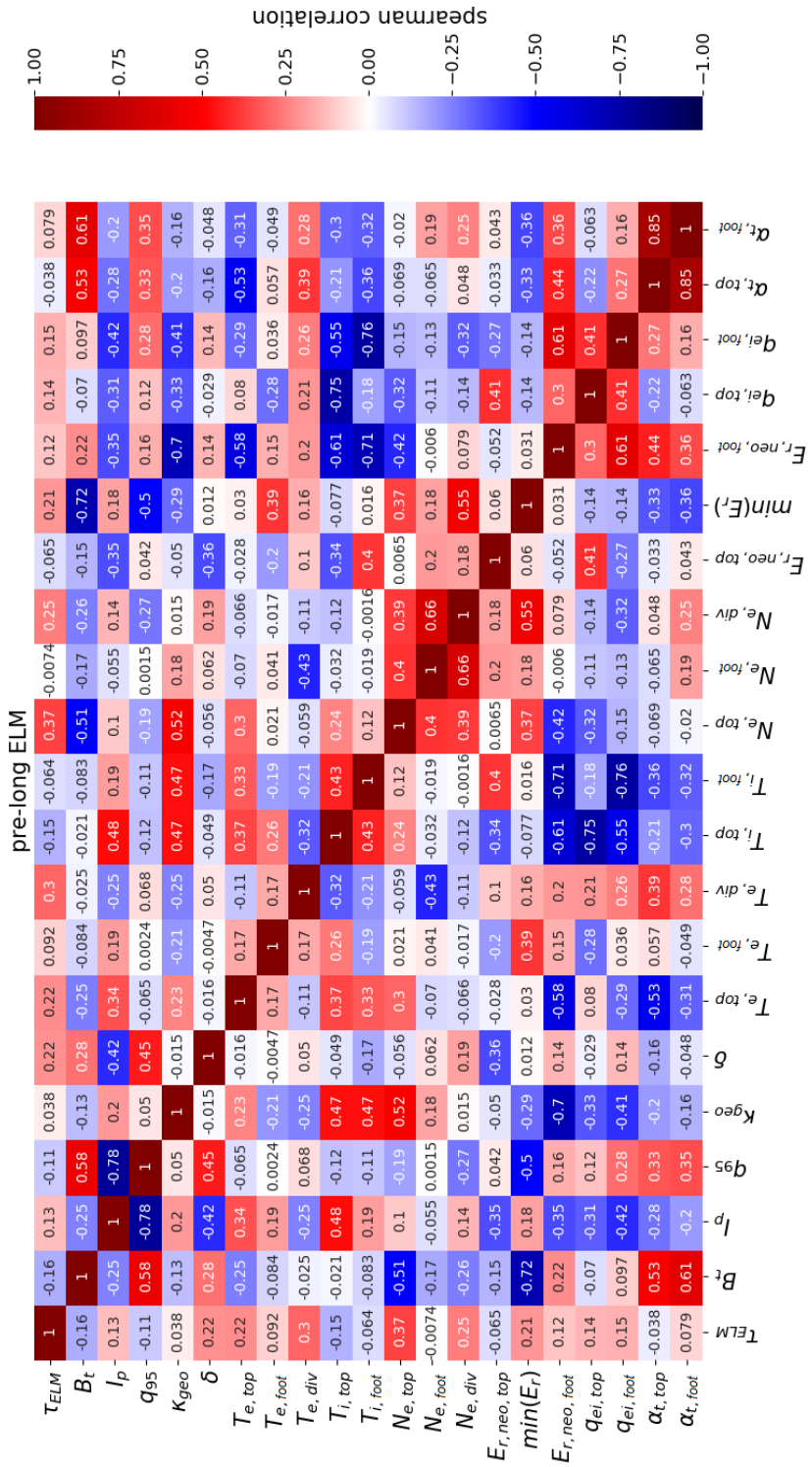

Figure 6.16: Illustration of the Spearman's rank correlation coefficient matrix considering only pre-long ELM values.

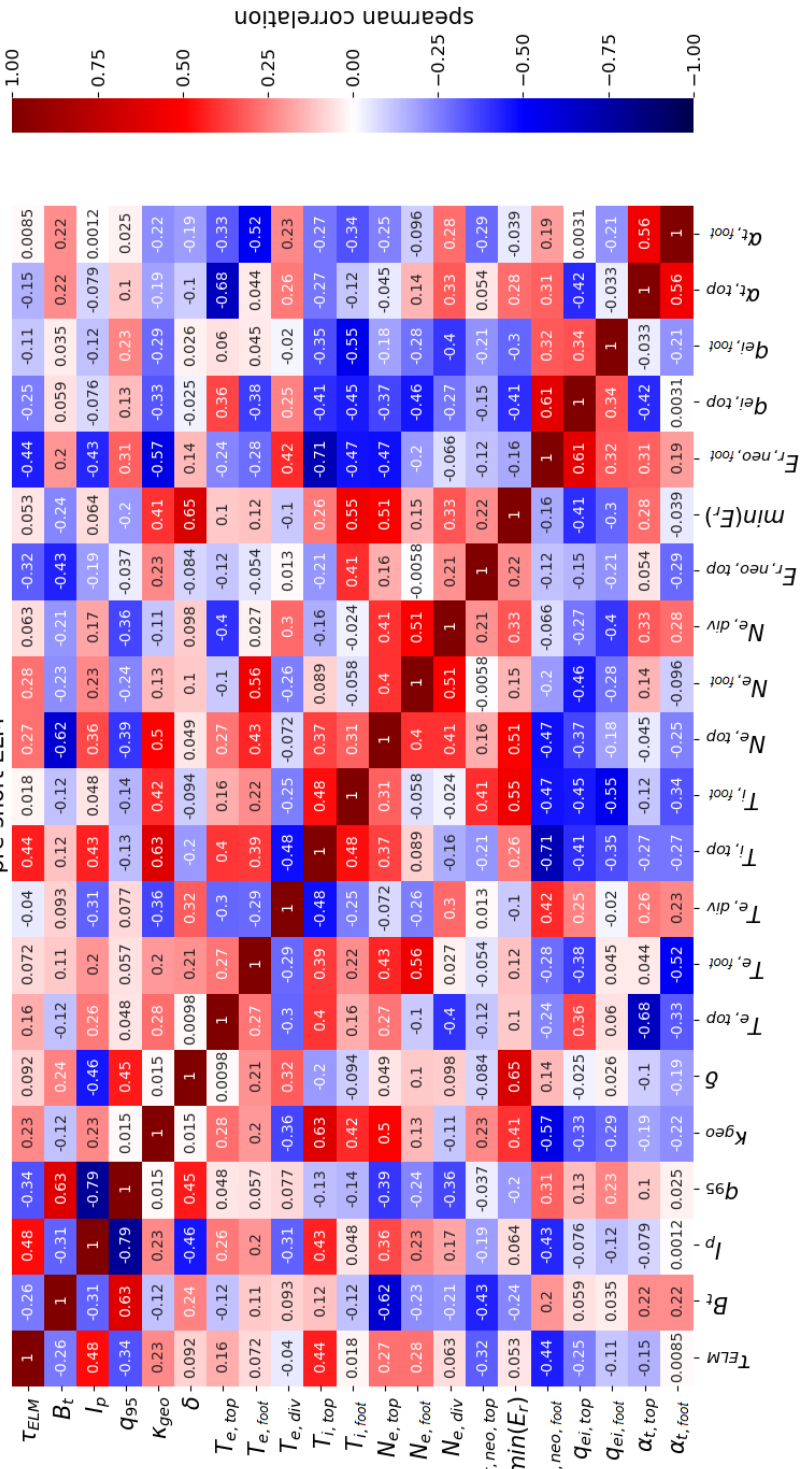

Figure 6.17: Illustration of the Spearman's rank correlation coefficient matrix considering only pre-short ELM values.

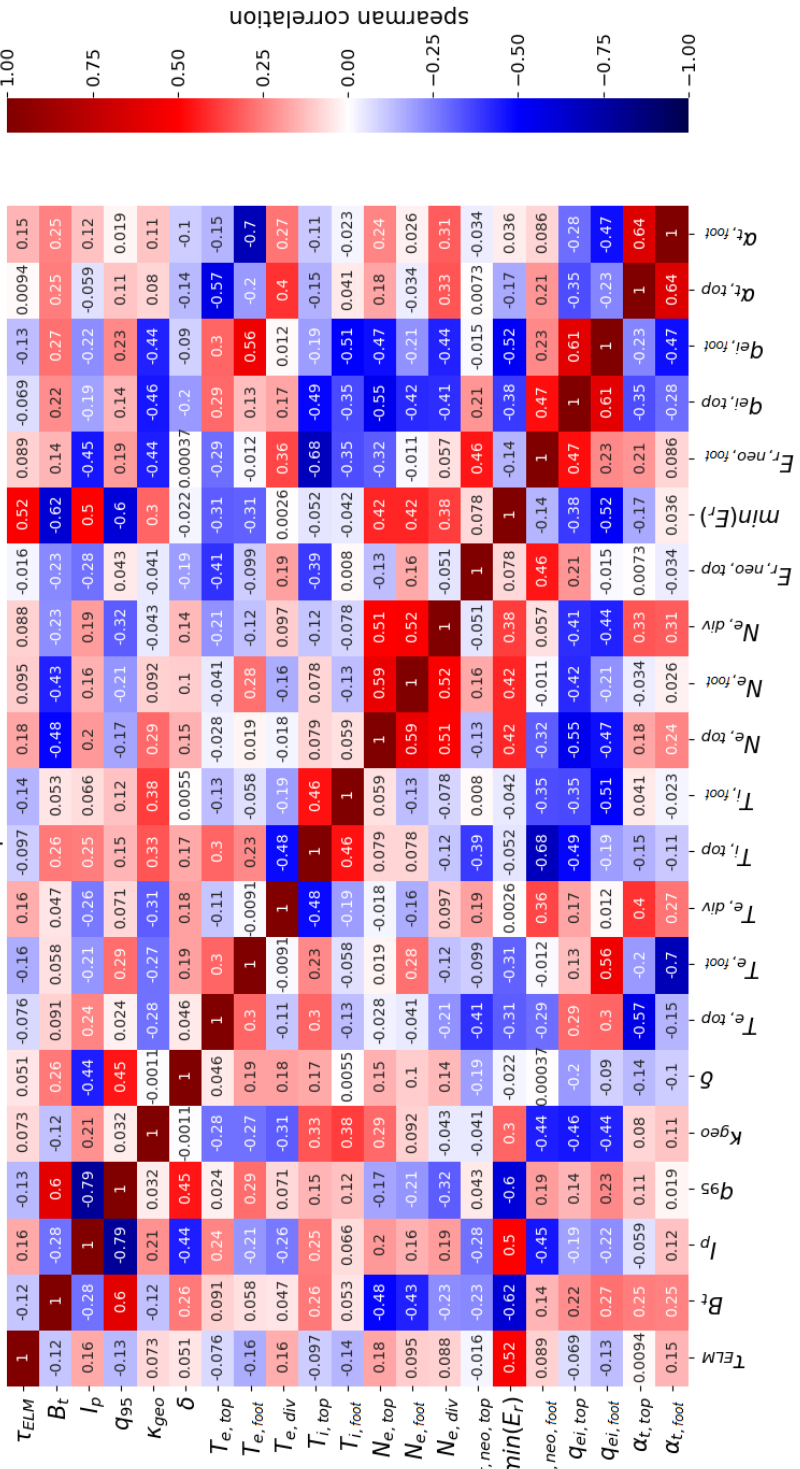

Figure 6.18: Illustration of the Spearman's rank correlation coefficient matrix considering only post-ELM values.

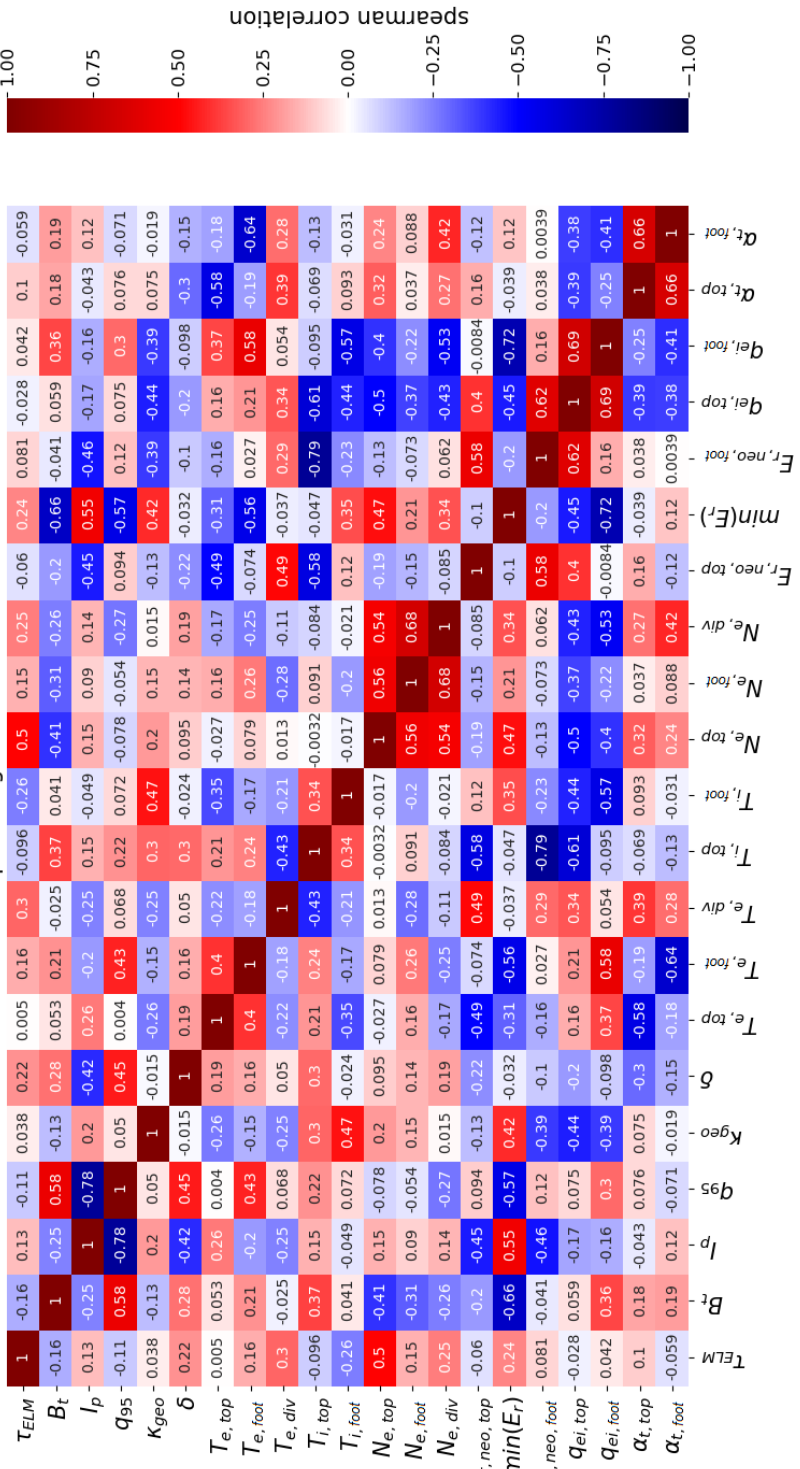

Figure 6.19: Illustration of the Spearman's rank correlation coefficient matrix considering only post-long ELM values.

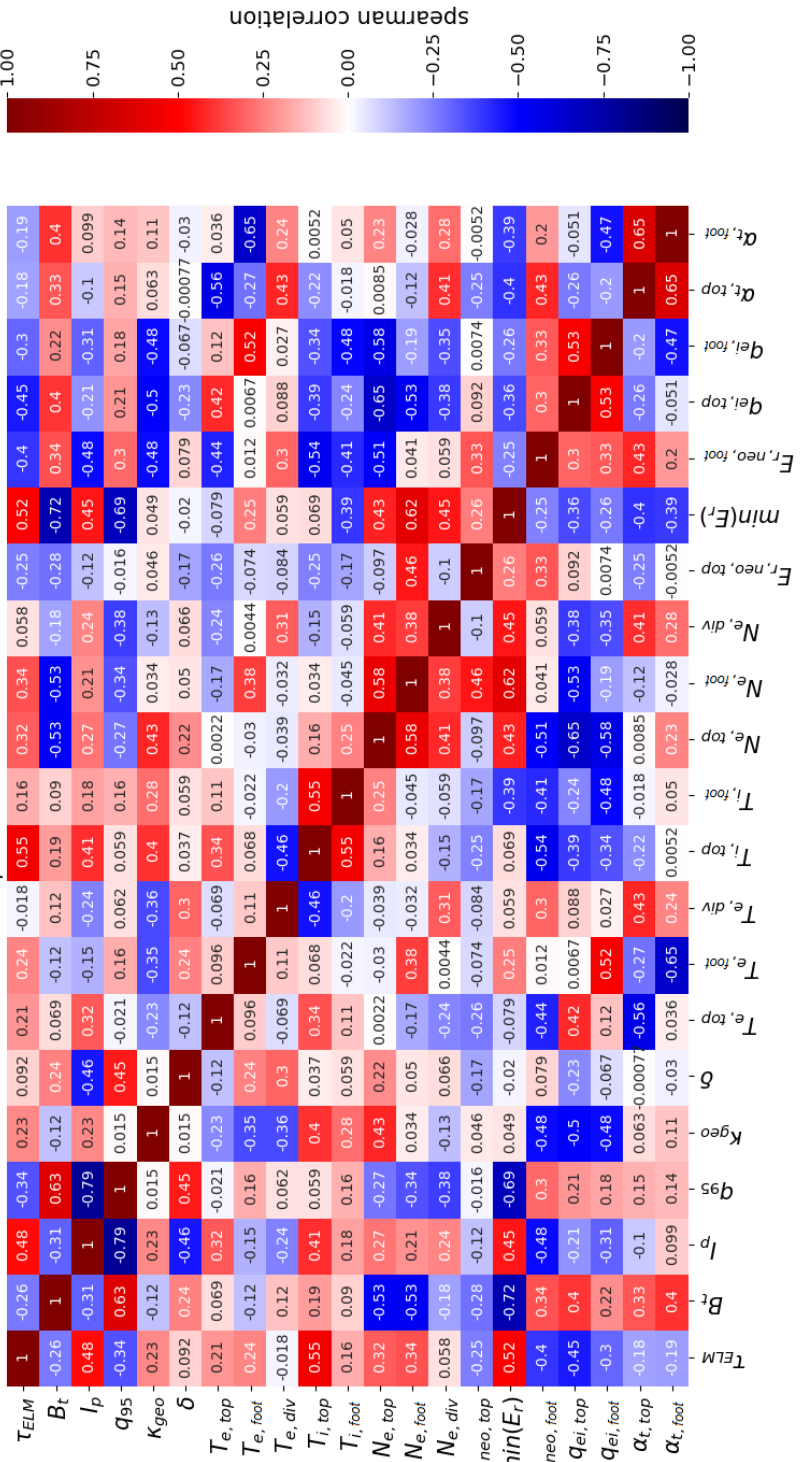

Figure 6.20: Illustration of the Spearman's rank correlation coefficient matrix considering only post-short ELM values.

7 Results and Discussion

This chapter discusses the observations described in chapter 6 and compares them to previous publications.

The main task of this thesis is the evaluation of the hypothesis regarding the ELM duration introduced in the first chapter. It states that during an ELM the absolute value of the radial electric field E_r collapses to values below 15 kV/m, which are typical for L-mode. Consequently, the ETB sustained by the radial electric field shear is thought to break down and strong filamentary transport is driven by the high pressure in the core. Only if E_r exceeds a critical value, the edge transport barrier builds up again and the strong transport can stop. However, it is demonstrated in figure 6.4 that not for all of the investigated cases, considering the radial electric field profiles during sufficiently long ELMs, the absolute value of $\min(E_r)$ lies under the limit of 15 kV/m. This is rather true only for half of the available cases. Hence the first part of the underlying hypothesis is inapplicable. Moreover, this seems to contradict the suggested mechanism in [53], which is a possible way inducing the second crash phase of an ELM, a short transition to L-mode. However, it is also shown in figure 6.5b that on average the absolute value of the minimum of the radial electric field profile tends to be bigger in size after short in comparison to after long ELMs. This observation goes along with the prediction of the underlying hypothesis.

Furthermore the underlying hypothesis claims that the collisional electron-ion-heat-exchange q_{ei} acts as critical parameter regulating the ELM duration. Only at high densities at which q_{ei} relevantly affects the ion temperature, the ion and electron temperature gradients are closely linked. Assuming dominant neoclassical ion transport the collisional electron-ion-heat-exchange at the separatrix sets the radial electric field indirectly through the ion temperature gradient and therefore regulates the ELM duration. However, on the whole figures 6.7 and 6.8 do not show higher q_{ei} values for short ELMs than for long ELMs, whereupon due to the especially high uncertainties a firm conclusion cannot be drawn. Nevertheless, the rough calculation comparing the total ion heat flux and the total collisional electron-ion-heat-exchange demonstrates that the total collisional electron-ion-heat-exchange can be neglected compared to the total ion heat flux. Consequently, the collisional electron-ion-heat-exchange at the separatrix appears not to be able to regulate the ELM duration. Together these two analyses contradict the second part of the underlying hypothesis of this thesis.

As already discussed above L. Frassinetti et al. found in [30] that on average the long ELMs seem to have higher pre-ELM divertor temperatures than the short ELMs and that the pre-ELM divertor temperature seems to be crucial in triggering the long ELMs. Considering the divertor data analysed in the scope of this thesis this trend cannot be retrieved, as the data in figure 6.3 corresponding to long and short ELMs overlap each

other within their uncertainties. Contrarily, the finding of the very same publication that there is no major difference between pre-long and pre-short ELM pedestal top values can be retrieved, as depicted in figure 6.1.

The turbulence control parameter α_t is, as previously described, a measure for the impact of the interchange effect on drift-wave turbulence and thereby describes the strength of the plasma edge turbulence and its transport. According to its composition it is linearly linked to the edge collisionality. It is shown in figure 6.12b that on average the long ELMs tend to have higher post-ELM α_t values. This trend is reinforced in figure 6.14b, where the size of post-ELM α_t at the pedestal foot seems to separate the long and the short ELMs. Moreover, an interplay with $\min(E_r)$ and additional impurity seeding cannot be excluded. These observations can be coherently interpreted in the following way: In general after short ELMs the absolute value of the radial electric field is relatively high. Hence the ETB is sustained and the edge turbulence and transport are suppressed, which corresponds to small α_t values. However, it is not possible to determine if the high -$\min(E_r)$ causes the low strength of edge turbulence and transport or if the establishment of a solid E_r is carried out due to small edge turbulence and transport. In the case of long ELMs the post-ELM absolute value of the radial electric field is smaller and at the same time the turbulence control parameter is higher. If additional impurities are seeded, the post-ELM (-$\min(E_r)$) and post-ELM α_t are for both ELM types smaller in size. P.A. Schneider et al. state in [31] that the consequence of nitrogen seeding is in most cases a reduction of n_e/T_e. This goes well along with the reduced turbulence control parameter values for intervals with additional gas seeding found here as $\alpha_t \propto n_e/T_e^2$. However, if for some reason beyond this picture the long ELMs have higher absolute values for the radial electric field, the turbulence control parameter can be smaller in size as well. As these relations are not trivial, they just cannot be observed in the correlation matrices in the figures 6.18, 6.19 and 6.20. The only exception is the seemingly indirect monotonic relation between α_t and $\min(E_r)$ for the post-short ELM case, which has been observed in figure 6.20. This could be interpreted as indication that an interplay between the edge turbulence or rather transport and the radial electric field regulates the ELM duration.

8 Summary and Outlook

The main scope of this thesis has been the examination of the hypothesis that during the ELM crash the absolute value of the radial electric field E_r collapses to typical L-mode values below 15 kV/m. Hence the ETB, which is sustained by the radial electric field shear, breaks down and enables strong filamentary transport until E_r builds up again. Furthermore it has been assumed that the collisional electron-ion-heat-exchange q_{ei} at a position close to the separatrix can relevantly affect the ion temperature, whose gradient enters the neoclassical prediction of the radial electric field. Therefore small ELMs have been expected if q_{ei} was big in size. Collectively 36 temporal intervals have been examined provided by 20 different ASDEX Upgrade H-mode discharges with type-I ELMs. For the calculation of q_{ei} and $E_{r,neo}$ ELM-synchronised electron density, ion temperature and electron temperature pedestal profiles have been evaluated. In order to separately obtain them for long and short ELMs, modules for the application development system FusionFit have been developed. Instead of using the divertor current signal as measure for the ELM onset and ending times an algorithm has been devised combining the divertor current and magnetic pick-up coil signals.

Within the uncertainties no correlation of the ELM duration and the collisional electron-ion-heat-exchange or the neoclassical prediction of the radial electric field could be observed. Further it has been estimated for discharge #36650 in the temporal interval [4.0 - 5.0]s that Q_{ei}/Q_i=0.0046, meaning that the total collisional electron-ion-heat-exchange Q_{ei} is about less than a two-hundredth of the total ion heat flux Q_i. Consequently, it is highly unlikely that the magnitude of the collisional electron-ion-heat-exchange suffices to relevantly affect the ELM duration. Using data from the highly resolving CXRS measurement system the examination of the radial electric field profiles during long ELMs was possible. In 10 out of 20 available profile data the minimum value of E_r lies under the limit of -15 kV/m. Consequently, the underlying hypothesis had to be falsified in total. Nevertheless, the actual prediction from the hypothesis of lower values of the minimum of the radial electric field for times after short ELMs in contrast to the ones after long ELMs could be confirmed regarding pedestal foot data. Moreover, regarding post-ELM pedestal foot data the observations tend to indicate that the post-ELM turbulence control parameter α_t at the pedestal foot acts as parameter separating the long from the short ELMs. Furthermore post-short ELM $\alpha_{t,foot}$ seems to scale with the absolute value of the minimum of the radial electric field. Therefore an interplay between the radial electric field and the edge turbulence or rather transport tends to regulate the occurrence of the second ELM crash phase and consequently the respective ELM duration.

However, the current understanding of the ELM duration regulation mechanism could be intensified by further investigation of the interplay between the turbulence control parameter α_t and the radial electric field E_r. This includes for instance to consider, how

the post-short ELM α_t values at the pedestal foot scale with the minimum of E_r. In order to do this a more fundamental analysis of the CXRS data would be beneficial. L. Frassinetti et al. showed in [30] that the losses of the first ELM phase are regulated by the pedestal collisionality. As according to its composition α_t is linearly linked to the edge collisionality, it is highly recommended to compare it with the ELM power losses of the different phases as well. In chapter 6 radial electric field profiles representing data during long ELMs have been presented. A deeper insight into the ELM duration regulating mechanism could also be gained by further highly resolved CXRS measurements, which provide radial electric field profiles during short ELMs.

This work is humbly aimed to be one out of innumerable contributions towards the understanding of plasma dynamics and practicable magnetically confined fusion and thereby to bring the realisation of the first nuclear fusion power plant providing carbon-free base load electricity in the future one tiny step closer.

A. Acknowledgements

With the conclusion of this thesis it is time for a few words thanking those, without whom this thesis would not have been possible:

Firstly, I want to thank my supervisor *Friedrich Aumayr*, who made this thesis possible in the first place, took me in as diploma student and put me in contact with the Max Planck Institute for Plasma Physics in Garching.
Secondly, my thanks go to *Elisabeth Wolfrum*, who came up with the idea of the main hypothesis of this thesis and took though her full schedule the time for weekly meetings to ensure highly qualitative supervision. Your curiosity regarding new findings and your visible enthusiasm with regard to training young academics has been highly inspiring!
Furthermore many thanks to *Georg Harrer*, who among other things has helped getting my thesis started by introducing me to the ASDEX Upgrade shotfile system and obtaining a broader overview of the different diagnostics!
Philip Schneider is the creator of FusionFit, which has been a helpful tool for the purposes of this thesis. I am especially grateful for your support of developing my own FusionFit user module!
Thank you *Marco Cavedon* for your scientific opinion about the origin of the different ELM durations, the help with the selection of the available discharges and for providing the radial electric field data!
I further thank *Rainer Fischer* for supplying Z_{eff} data, *Dominik Brida* for your standard program of reading the divertor data, which has been a great basis for the adaption to my own needs and *Christian Schuster* for sharing your knowledge about the ion heat flux at the plasma edge.
I also thank *Florian* and *Markus* for the scientific discussions in the supervising meetings regarding *Florian's* bachelor thesis, as these generated some further ideas for my own thesis.
Lastly, I want to thank *Gerald Kamelander*, whose plasma-physics-lecture has been the first opportunity to deepen my interest regarding nuclear fusion and who encouraged me to inquire *Friedrich Aumayr* about a possible thesis.

Eventually, I want to thank the core group of the physicist *Cornelia*, *Barbara*, *Peter* and *Julian* with whom our friendship partially goes back to *Grundlagen der Physik I.*
Further thanks go to my sister *Alexandra* for the shared culinary breaks to clear our minds in numerous evenings.
I also thank *Eugenie* for understanding that weekends were dedicated to things like solving *E-Dyn. tasks or whatever* and for being nothing but supportive throughout my entire studies.
Finally, I want to thank my parents *Gerda* and *Christian* for encouraging my curiosity and interests as a child, for always appraising our education the highest significance and for all of your support!

B. Bibliography

[1] EUROfusion. *Fusion Plant*. 2014. URL: https://www.iter.org/doc/www/content/com/Lists/WebText_2014/Attachments/183/fusion_plant.jpg. (accessed 5.4.2021).

[2] ITER Organization. *Advantages of Fusion*. 2021. URL: https://www.iter.org/sci/Fusion. (accessed 5.4.2021).

[3] A. Donne. "The European roadmap towards fusion electricity". *Philosophical Transactions of the Royal Society A: Mathematical, Physical and Engineering Sciences* 377.2141 (2019), p. 20170432. DOI: 10.1098/rsta.2017.0432.

[4] W. Bahm, I. Milch, and R.P. Schorn. *Kernfusion*. 2006. URL: http://www.fusion.kit.edu/downloads/Kernfusion.pdf. (accessed 27.3.2021).

[5] G. McCracken and P. Stott. *Fusion*. Academic Press, 2005, pp. 14–15, 38, 43. ISBN: 978-0-12-481851-4.

[6] M. Decréton et al. *Controlled nuclear fusion: the energy of the stars on earth - white paper on fusion energy*. SCK CEN Reports BLG-1049. Studiecentrum voor Kernenergie, 2007, p. 16.

[7] J. Wesson et al. *Tokamaks*. 3rd edition. Oxford University Press, 2004, pp. 4, 67–69, 514–518, 546. ISBN: 0-19-8509227.

[8] Wikimedia Foundation. *Fusion in the Sun*. 2016. URL: https://commons.wikimedia.org/wiki/File:Fusion_in_the_Sun.svg#metadata. (accessed 29.3.2021).

[9] ITER Organization. *What is a tokamak?* 2021. URL: https://www.iter.org/mach/Tokamak. (accessed 30.3.2021).

[10] G. Kamelander. *Grundlagen der Plasmaphysik mit besonderer Berücksichtigung der Fusionsphysik*. Personal Collection of G. Kamelander, Technische Universität Wien, 2017, pp. 31, 38–40, 58–61, 140.

[11] Max-Planck-Gesellschaft zur Förderung der Wissenschaften e.V. *Tokamak principle*. 2011. URL: https://www.euro-fusion.org/news/detail/?tx_news_pi1%5Bnews%5D=386&cHash=77c6bbd22b8e74ad074890e63944f9f7. (accessed 30.3.2021).

[12] U. Stroth. *Plasmaphysik*. 2nd edition. Springer Spektrum, 2018, pp. 116, 365–366, 524–529. ISBN: 978-3-662-55235-3.

[13] M. Cavedon. "The role of the radial electric field in the development of the edge transport barrier in the ASDEX Upgrade tokamak". *Dissertation (Technische Universität München)* (2016), pp. 3, 34–36.

[14] F. Wagner et al. "Regime of Improved Confinement and High Beta in Neutral-Beam-Heated Divertor Discharges of the ASDEX Tokamak". *Physical Review Letters* 49 (1982), pp. 1408–1412. DOI: 10.1103/PhysRevLett.49.1408.

[15] M. Keilhacker. "H-mode confinement in tokamaks". *Plasma Physics and Controlled Fusion* 29.10A (1987), pp. 1401–1413. DOI: 10.1088/0741-3335/29/10a/320.

[16] F. Wagner et al. "Importance of the divertor configuration for attaining the H-regime in ASDEX". *Journal of Nuclear Materials* 121 (1984), pp. 103–113. DOI: 10.1016/0022-3115(84)90109-0.

[17] F. Wagner et al. "Development of an Edge Transport Barrier at the H-Mode Transition of ASDEX". *Physical Review Letters* 53 (1984), pp. 1453–1456. DOI: 10.1103/PhysRevLett.53.1453.

[18] G.F. Harrer. "On the origin and transport of small ELMs". *Dissertation (Technische Physik Wien)* (2020), p. 9.

[19] H. Zohm. "Edge localized modes (ELMs)". *Plasma Physics and Controlled Fusion* 38.2 (1996), pp. 105–128. DOI: 10.1088/0741-3335/38/2/001.

[20] G. Federici, A. Loarte, and G. Strohmayer. "Assessment of erosion of the ITER divertor targets during type I ELMs". *Plasma Physics and Controlled Fusion* 45.9 (2003), pp. 1523–1547. DOI: 10.1088/0741-3335/45/9/301.

[21] W. Suttrop. "The physics of large and small edge localized modes". *Plasma Physics and Controlled Fusion* 42.5A (2000), A1–A14. DOI: 10.1088/0741-3335/42/5a/301.

[22] H. Zohm for the ASDEX Upgrade Team and the EUROfusion MST1 Team. "Recent ASDEX Upgrade research in support of ITER and DEMO". *Nuclear Fusion* 55.10 (2015), p. 104010. DOI: 10.1088/0029-5515/55/10/104010.

[23] Max-Planck-Gesellschaft zur Förderung der Wissenschaften e.V. *Detailed description of ASDEX Upgrade*. 2020. URL: https://www.aug.ipp.mpg.de/wwwaug/documentation/physics/techdata.shtml. (accessed 30.3.2021).

[24] E. Wolfrum. Personal communication, 2020.

[25] M. Cavedon. Personal communication, 2020.

[26] M. Dibon. *Fotos, Grafiken ASDEX Upgrade*. 2021. URL: https://www.ipp.mpg.de/844131/asdex_upgrade. (accessed 30.3.2021).

[27] H. Biglari, P. H. Diamond, and P. W. Terry. "Influence of sheared poloidal rotation on edge turbulence". *Physics of Fluids B: Plasma Physics* 2.1 (1990), pp. 1–4. DOI: 10.1063/1.859529.

[28] P. Manz, M. Ramisch, and U. Stroth. "Physical Mechanism behind Zonal-Flow Generation in Drift-Wave Turbulence". *Phys. Rev. Lett.* 103 (2009), p. 165004. DOI: 10.1103/PhysRevLett.103.165004.

[29] P. A. Schneider et al. "Observation of different phases during an ELM crash with the help of nitrogen seeding". *Plasma Physics and Controlled Fusion* 56.2 (2014), p. 025011. DOI: 10.1088/0741-3335/56/2/025011.

[30] L. Frassinetti et al. "ELM behavior in ASDEX Upgrade with and without nitrogen seeding". *Nuclear Fusion* 57.2 (2016), p. 022004. DOI: 10.1088/0029-5515/57/2/022004.

[31] P. A. Schneider et al. "Pedestal and edge localized mode characteristics with different first wall materials and nitrogen seeding in ASDEX Upgrade". *Plasma Physics and Controlled Fusion* 57.1 (2014), p. 014029. DOI: 10.1088/0741-3335/57/1/014029.

[32] M. Cavedon et al. "Pedestal and Er profile evolution during an edge localized mode cycle at ASDEX Upgrade". *Plasma Physics and Controlled Fusion* 59.10 (2017), p. 105007. DOI: 10.1088/1361-6587/aa7ad0.

[33] A. Burckhart et al. "Inter-ELM behaviour of the electron density and temperature pedestal in ASDEX Upgrade". *Plasma Physics and Controlled Fusion* 52.10 (2010), p. 105010. DOI: 10.1088/0741-3335/52/10/105010.

[34] E. Viezzer et al. "High-accuracy characterization of the edge radial electric field at ASDEX Upgrade". *Nuclear Fusion* 53.5 (2013), p. 053005. DOI: 10.1088/0029-5515/53/5/053005.

[35] B. N. Rogers, J. F. Drake, and A. Zeiler. "Phase Space of Tokamak Edge Turbulence, the $L-H$ Transition, and the Formation of the Edge Pedestal". *Phys. Rev. Lett.* 81 (1998), pp. 4396–4399. DOI: 10.1103/PhysRevLett.81.4396.

[36] B. D. Scott. "Drift wave versus interchange turbulence in tokamak geometry: Linear versus nonlinear mode structure". *Physics of Plasmas* 12.6 (2005), p. 062314. DOI: 10.1063/1.1917866.

[37] B. D. Scott. "Tokamak edge turbulence: background theory and computation". *Plasma Physics and Controlled Fusion* 49.7 (2007), S25–S41. DOI: 10.1088/0741-3335/49/7/s02.

[38] B. D. Scott. "The nonlinear drift wave instability and its role in tokamak edge turbulence". *New Journal of Physics* 4 (2002), pp. 52–52. DOI: 10.1088/1367-2630/4/1/352.

[39] W. M. Stacey. *Fusion Plasma Physics*. 2nd edition. WILEY-VCH, 2012, p. 195. ISBN: 978-3-527-40586-2.

[40] T. Eich et al. "Turbulence driven widening of the near-SOL power width in ASDEX Upgrade H-Mode discharges". *Nuclear Fusion* 60.5 (2020), p. 056016. DOI: 10.1088/1741-4326/ab7a66.

[41] T. Eich and P. Manz. "The separatrix operational space of ASDEX Upgrade due to interchange-drift-Alfven turbulence". *Nuclear Fusion* (2021). accepted manuscript.

[42] A. W. DeSilva. "The evolution of light scattering as a plasma diagnostic". *Contrib. Plasma Phys* 40.12 (2000). DOI: 10.1002/(SICI)1521-3986(200004)40:1/2<23::AID-CTPP23>3.3.CO;2-Z.

[43] N.J. Peacock et al. "Measurement of the Electron Temperature by Thomson Scattering in Tokamak T3". *Nature* 224.5218 (1969), pp. 488–490. DOI: 10.1038/224488a0.

[44] B. Kurzan and H. D. Murmann. "Edge and core Thomson scattering systems and their calibration on the ASDEX Upgrade tokamak". *Review of Scientific Instruments* 82.10 (2011), p. 103501. DOI: 10.1063/1.3643771.

[45] R. J. Fonck, D. S. Darrow, and K. P. Jaehnig. "Determination of plasma-ion velocity distribution via charge-exchange recombination spectroscopy". *Phys. Rev. A* 29 (6 1984), pp. 3288–3309. DOI: 10.1103/PhysRevA.29.3288.

[46] M. Cavedon et al. "A fast edge charge exchange recombination spectroscopy system at the ASDEX Upgrade tokamak". *Review of Scientific Instruments* 88.4 (2017), p. 043103. DOI: 10.1063/1.4979801.

[47] M. Weinlich. "Elektrostatische Sonden in starken Magnetfeldern". *Dissertation (Technische Universität München)* (1995), pp. 7–9.

[48] A. Kallenbach et al. "Electric currents in the scrape-off layer in ASDEX Upgrade". *Journal of Nuclear Materials* 290-293 (2001), pp. 639–643. DOI: 10.1016/S0022-3115(00)00445-1.

[49] P. C. Stangeby. *The Plasma Boundary of Magnetic Fusion Devices*. Institute of Physics Publishing, 2000, pp. 221–230. ISBN: 0-7503-0559-2.

[50] A. Kallenbach et al. "Multi-machine comparisons of H-mode separatrix densities and edge profile behaviour in the ITPA SOL and Divertor Physics Topical Group". *Journal of Nuclear Materials* 337-339 (2005), pp. 381–385. DOI: 10.1016/j.jnucmat.2004.10.099.

[51] E. Viezzer et al. "Ion heat and momentum transport in the edge pedestal of ASDEX Upgrade". *42nd EPS Conference on Plasma Physics, Lisbon, Portugal* (22nd to 26th June, 2015).

[52] E. Viezzer et al. "Evidence for the neoclassical nature of the radial electric field in the edge transport barrier of ASDEX Upgrade". *Nuclear Fusion* 54.1 (2013), p. 012003. DOI: 10.1088/0029-5515/54/1/012003.

[53] H. Zohm et al. "ELM studies on DIII-D and a comparison with ASDEX results". *Nuclear Fusion* 35.5 (1995), pp. 543–550. DOI: 10.1088/0029-5515/35/5/i05.